Characterization of the 1966 Camp Century Sub-Glacial Core: A Multiscale Analysis

Catherine M. Collins[1], Nicolas Perdrial[1,2], Pierre-Henri. Blard[3,4], Nynke Keulen[5], William C. Mahaney[6], Halley Mastro[1], Juliana Souza[1], Donna M. Rizzo[7], Yves Marrocchi[3], Paul C. Knutz[5], Paul R. Bierman[1]

5 [1]Rubenstein School of Environment and Natural Resources, University of Vermont, Burlington, VT, USA
[2]Department of Geography & Geosciences, University of Vermont, Burlington, VT, USA
[3]Centre de Recherches Pétrographiques et Géochimiques, Centre national de la recherche scientifique, UMR 7358, Vandœuvre-lès-Nancy 54501, France
[4]Université Libre de Bruxelles, Laboratoire de Glaciologie, ULB, Brussels, 1050, Belgium
10 [5]Geological Survey of Denmark and Greenland, 1350 Copenhagen, Denmark
[6]Quaternary Surveys, 26 Thornhill Ave., Thornhill, ON L4J1J4, Canada
[7]Department of Civil and Environmental Engineering, University of Vermont, Burlington, VT, USA

Correspondence to: Catherine Collins (catmcollins17@gmail.com)

Abstract. In 1966, drilling at Camp Century, Greenland, recovered 3.44 meters of sub-glacial material from beneath 1350
15 meters of ice. Although prior analysis of this material showed that the core includes glacial sediment, ice, and sediment deposited during an interglacial, the sub-glacial material had never been thoroughly studied. To better characterize this material, we analyzed 26 of the 30 core samples remaining in the archive. We performed a multi-scale analysis including X-ray diffraction, micro-computed tomography, and scanning electron microscopy to delineate stratigraphic units and assign facies based on inferred depositional processes.

20 At the macro-scale, quantitative X-ray diffraction revealed that quartz and feldspar dominated the sediment and that there was insignificant variation in relative mineral abundance between samples. Meso-scale evaluation of the frozen material using micro-computed tomography scans showed clear variations in the stratigraphy of the core characterized by the presence of bedding, grading, and sorting. Micro-scale grain size and shape analysis, conducted using scanning electron microscopy, showed an abundance of fine-grained materials in the lower part of the core and no correspondence between grain shape
25 parameters and sedimentary structures. These multiscale data define 5 distinct stratigraphic units within the core based on sedimentary process; K-means clustering analysis supports this proposed unit delineation. Our observations suggest that ice retreat uncovered the Camp Century region exposing basal till, covered with a remnant of basal ice or firn (Units 1 and 2). Continued ice-free conditions led to till disruption by liquid water causing a slump deposit (Unit 3) and the development of a small fluvial system of increasing energy up core (Units 4-5).

30 Analysis of the Camp Century sub-glacial material indicates a diverse stratigraphy preserved below the ice that recorded episodes of glaciated and deglaciated conditions in northwestern Greenland. Our physical, geochemical, and mineralogic analyses reveal a history of deposition, weathering, and sediment transport preserved under the ice and show the promise of sub-glacial materials to increase our knowledge of past ice sheet behavior over time.

1 Introduction

35   Understanding past ice-free times allows us to predict the response of the Greenland Ice Sheet (GrIS) to current and future climate warming (Gemery & López-Quirós, 2024). This goal, deciphering Greenland's paleoclimate and ice sheet stability, has driven the ice core collection efforts since the 1950s (Bader, 1962). Deep ice coring in Greenland began in 1960 at Camp Century, a military camp in northwestern Greenland, ~200 km inland from the ice margin (Langway, 2008) (Fig. 1). The creation of this camp was one of many American responses to the perceived Russian threat in the arctic during the Cold
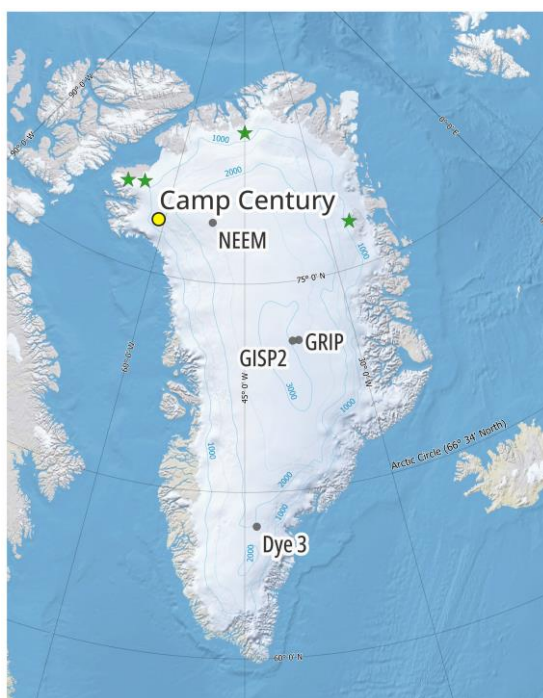
40   War (Clark, 1965).

Figure 1. Map of Greenland (Harrison et al., 2011; Moon et al., 2023) **showing drilling locations where sub-glacial material has been retrieved. Drilling locations for ongoing GreenDrill project (Prudhoe Land, Hiawatha Margin, Victoria Fjord, and Dronning Louise from West to East) are marked by a green star.**

At Camp Century (77.2°N, 61.1°W), the U.S. Army drilled the first deep ice core that entirely penetrated an ice sheet.

45   Additionally, they collected 3.44 m of sub-glacial material which would be the largest sub-glacial archive for the next six decades (Balter-Kennedy et al., 2023; Langway, 2008). The ice from this core was studied extensively (e.g., Hansen & Langway, 1966a; Johnsen et al., 1972; Langway & Hansen, 1970; W. Dansgaard et al., 1969)) but the sub-glacial material was left relatively untouched save for a handful of studies (Fountain et al., 1981; Harwood, 1986; Whalley & Langway, 1980). The sub-glacial material did not move to the US Ice Core Repository with the rest of Camp Century core in the mid-1990s and was

50   thought, by US researchers, to have been lost. It's rediscovery in 2019 in freezers of the Niels Bohr Institute at the University of Copenhagen sparked new interest in analyzing this unique archive (Bierman et al., 2024; Voosen, 2019).

The Camp Century sub-glacial core contains 3.44 meters of basal materials (Hansen & Langway, 1966b). It is made up of several units, the deepest containing sediment last exposed to sunlight and cosmic radiation between 1.5-3.2 Myr (Bierman et al., 2024; Christ et al., 2021). Data show that the top of the core was exposed at the surface 416,000±38,000 years ago, which places its last exposure during a deglaciation that occurred during Marine Isotope Stage (MIS) 11 (Christ et al., 2021, 2023). MIS 11 (374 to 424 ka) was both a long and warm interglacial with a peak atmospheric CO_2 concentration similar to pre-industrial levels (Dutton et al., 2015). This makes MIS 11 an important but imperfect analogue by which to study the effects of future warming and GrIS stability (Dutton et al., 2015; Jouzel et al., 2007; Lisiecki & Raymo, 2005; Lüthi et al., 2008; Robinson et al., 2017). The presence of plant and invertebrate fossils in the Camp Century sub-glacial core mandates the site was not covered by ice during MIS 11 and indicates the maximum limit for ice extent at that time (Christ et al., 2021, 2023).

In this study, we used multiple physical, geochemical, and mineralogic techniques to characterize 26 of the 30 existent samples cut from the 3.44-meter Camp Century sub-glacial sediment core (Bierman et al., 2024). Our analyses refine the understanding of sub-glacial materials collected from below the GrIS at Camp Century in 1966. We employed a multi-scale technique to define sequence stratigraphy and analyze facies to infer what environments were present when this sediment and ice were deposited. At the macro-scale, we conducted a mineralogical survey using X-ray diffraction (XRD) to quantify relative mineral assemblages. At the meso-scale, we used non-destructive micro-computed tomography (µCT) of the frozen sediment to make detailed stratigraphic observations at the tens of microns scale. We also used scanning electron microscopy (SEM) and associated geochemical mapping to analyze grain coatings, textures, and shapes at the micron scale. Using non-destructive µCT in tandem with other methods (XRD, SEM) allowed us to maximize data output when working with a volumetrically limited archive. Characterizing this unique sub-glacial core offers the opportunity to expand our knowledge of Greenland's climatic history, interglacial surface processes, and sub-glacial processes in addition to demonstrating the potential for subglacial materials to inform our understanding of ice sheet behavior over time.

2 Background

Sub-glacial material is a valuable source of both paleoclimate and glacial process information (e.g., Bierman et al., 2014; Schaefer et al., 2016). Sediment preserved beneath the ice and in basal ice can reveal crucial information about ice-free events, their duration, and specific surface processes. Basal materials are particularly important because they contain in-situ physical evidence for past events that are not recorded in glacier ice (Bender et al., 2010; Bierman et al., 2014; Blard et al., 2023; Christ et al., 2021, 2023; Gow & Meese, 1996; Marschalek et al., 2024; Schaefer et al., 2016; Suwa et al., 2006; Yau et al., 2016).

2.1 Basal Ice

Nearly every deep ice core from the GrIS (Camp Century, Dye 3, Greenland Ice Sheet Project - GISP2, Greenland Ice Core Project - GRIP, and North Eemian Project - NEEM) has retrieved meters of deformed ice containing bed material,

referred to as silty ice or basal ice (e.g., Bender et al., 2010; Blard et al., 2023; Christ et al., 2021; Gow & Meese, 1996; Hansen
85   & Langway, 1966a; Souchez et al., 1998; Suwa et al., 2006). The basal ice layers (BIL), found above the ice-bed interface, are
influenced by processes operating at and near the bed – specifically deformation, regelation, and in some cases melting. This
limits the interpretability of the climate record in the deepest ice, but the sediments entrained in the basal ice can reflect aspects
of glacial and sub-glacial processes as well as paleoenvironmental conditions during ice-free episodes (Knight, 1997).

Initial analyses of debris in the Camp Century BIL confirmed, using SEM and XRD analysis, that the sediment
90   originated from the frozen material below (Herron et al., 1979). In other cores, investigation of ancient biomolecules in Dye 3
and GRIP silty ice found evidence that a boreal forest once existed at Dye 3 which necessitates extensive ice sheet retreat from
southern Greenland (65.2°N), but such retreat did not appear to reach as far north as GRIP (72.5°N) (Willerslev et al., 2007).
Stable water isotope composition of the BIL in the GRIP core, corroborated by a comparative study between the debris found
there and at GISP2 (72.5°N), indicates that the BIL originated as ground ice before incorporation into the larger growing ice
95   sheet and has since deformed (Gow et al., 1997; Gow & Meese, 1996; Souchez et al., 1994, 1995; Tison et al., 1994). A
multiproxy analytical approach applied to sediment in the BIL from the NEEM core (77.5°N) (Blard et al., 2023) found
evidence of a sequence of glacial retreat and advance possibly similar to that which has been identified in the Camp Century
sub-glacial material (Christ et al., 2021, 2023).

2.2 Sub-glacial Material

100   In Greenland, coring activities at Camp Century, GISP2, and GreenDrill retrieved sub-glacial material from beneath
the ice-bed interface (Balter-Kennedy et al., 2023; Christ et al., 2021; Gow & Meese, 1996; Souchez et al., 1994, 1998). At
GISP2, drillers extracted 48 cm of till (mostly boulders, only 8-10 cm fine grain material) and 1.07 m of underlying rock (Gow
et al., 1997). Cosmogenic isotopic analysis of that rock and till shows that the land surface at GISP2 was deglaciated for
extended periods of time during at least one and possibly many Pleistocene interglacials after the Mid Pleistocene Transition,
105   ~1.1 Ma (Bierman et al., 2023; Schaefer et al., 2016). Grain texture analysis of Camp Century sediments (Whalley & Langway,
1980) revealed two populations of grains mixed sub-glacially: angular grains, attributed to glacial crushing, and rounded
grains, attributed to aeolian transport. Whalley & Langway (1980) infer that the aeolian fraction must have been produced
before the ice advanced, mandating prior ice-free conditions. A petrographic investigation of 17 clasts in the Camp Century
sub-glacial core revealed that they were compositionally similar to those cropping out at the ice sheet margin (Fountain et al.,
110   1981). Extraction of fresh-water diatoms from the bottom of the Camp Century BIL and the upper part of the sub-glacial core
indicates that the ice retreated far enough to expose the Camp Century drill site at least once during the Pleistocene (Harwood,
1986). Cosmogenic and luminescence dating of the upper and lowermost sub-glacial samples show that the 3.44 m of material
records at least two glaciations separated by ice-free conditions during MIS11 (Christ et al., 2021, 2023). The currently active
northern Greenland drilling project, GreenDrill, has successfully retrieved 3 m of silt to cobble-sized sediment in basal ice
115   atop 4.5 m of gneiss bedrock (Balter-Kennedy et al., 2023; Briner et al., 2022).

2.3 Computed Tomography Stratigraphy

Computed tomography (CT), a technology widely used in the medical field, is also a powerful tool for examining sediment cores non-destructively (Renter, 1989). CT scans produce greyscale images based on the intensity of the attenuated X-ray beam (i.e., CT number) and are reconstructed to produce 3-dimensional (3D) models of the scanned object (Razi et al., 2014). CT scans have been used to do quantitative facies characterization by comparing density plots that suggest environmental changes (Emmanouilidis et al., 2020; Lee et al., 2021). Used in studying marine sediment cores, CT scans aid in calculating bulk density and its spatial variation vertically and laterally (Orsi et al., 1994). CT scans also provide detailed visualizations of sediment structures, grain distribution, and material densities (Mena et al., 2015).

CT scanning technologies are effective in studying frozen permafrost cores. Some studies have characterized the sediment properties, cryostructures, and ground ice content of permafrost but did not find CT successful as a proxy for identifying ground ice origin (Calmels & Allard, 2008; Lapalme et al., 2017). Micro CT (µCT), a refinement of this technology, provides micron-scale resolution (typically between 1-150 µm voxels) for more detailed studies and has been used to make pore-scale observations (Lei et al., 2018, 2022). Three-dimensional microstructure analysis in permafrost allows for quantification of physical properties, including the spatial density of ice inclusions, which can be useful in estimates of thermal conductivity (Nitzbon et al., 2022). The same authors suggest that microstructure analysis from µCT scans, in combination with other measurements, allows for reliable inference of depositional processes (Nitzbon et al., 2022).

2.4 Microscale Grain Characteristics

Grain characteristics have been used routinely to inform sedimentological studies (Naqshband & McElroy, 2016). Grain size distribution is understood to be an indicator of transport energy, as higher energy fluids can transport larger/heavier grains (Gresina et al., 2023; Hjulström, 1935; Malusà et al., 2016). Specific grain morphology, including roundness and circularity, are related to transport energy, transport distance, mode of transport, and conditions at the site of deposition (Krumbein, 1941). Recently, studies of grain morphology have used automated image analysis (Gresina et al., 2023; ;;; Szmańda & Witkowski, 2021; Tafesse et al., 2013) to infer transport mechanisms. For example, properties of particle shape, investigated using this method, correlate circularity and roundness with transport distance and energy, respectively (Gresina et al., 2023). Image analysis of sediment grains from coastal dunes shows that roundness and patterns in size and shape indicate various and specific modes of transport in aeolian sediments (van Hateren et al., 2020). Quartz morphology, including roundness assessments and microstructures, has revealed evidence of past storm frequency and has been used to reconstruct sediment provenance and transport in NW Poland during the Last Glacial Maximum (Kalińska-Nartiša et al., 2018; Woronko et al., 2015). Grain size analyses of loess deposits identify episodes of rapid climate change, which mimic rapid climate fluctuations during the last glacial period (Dansgaard-Oeschger events) that have been found in ice cores (Vandenberghe & Nugteren, 2001). Applied to glacially derived sediments, Lepp et al. (2024) recently showed that glacial and fluvial surface textures are retained on silt-sized quartz grains and can be used to evaluate sediment transport processes.

5

Grain coating abundance and distribution can also provide information of source conditions, erosional processes, original transport mechanism, and post-depositional pedogenic processes. Coatings on grain surfaces indicate post-depositional weathering and pore fluid transport of solids and solutes in both temperate and in Arctic regions (Dixon et al., 2002). Notably, the absence of grain coatings signals an active transport environment (Musselman & Tarbox, 2013). Glacial flour is also common in till and glacial lacustrine deposits and is characterized by agglomerates of clay- to silt-sized angular particles (Pesch et al., 2022) and small particles adhered to grain surfaces that have features consistent with glacial grinding (Mahaney, 2002; Whalley & Langway, 1980).

2.5 Cryostratigraphy

Cryostratigraphy describes the shape, amount, and distribution of ice and sediment in frozen ground (Gilbert et al., 2016; Murton & French, 1994). Cryofacies are defined by distinct patterns of ice lenses, volumetric ice content, and layering of ice and sediment. Cryostratigraphy helps infer permafrost formation mechanisms as either *epigenetic*, permafrost that forms after sediment deposition, or *syngenetic*, permafrost that forms as material is being deposited (French & Shur, 2010). Ground ice includes pore ice and segregated ice but typically excludes buried ice (French & Shur, 2010; Murton & French, 1994). Pore ice works as cement, holding the sediment together. Segregated ice forms as ice accumulates along the freezing plane, the boundary between conditions supporting liquid water and ice, and can be millimeters to tens of meters thick (French & Shur, 2010). Organized lenticular and layered cryostructures are common in syngenetic permafrost and tend to be short, thin, and highly abundant (French & Shur, 2010; Murton & French, 1994). Epigenetic permafrost is typically ice-poor, contains pore-filled cryostructures (Gilbert et al., 2016; Stephani et al., 2014) and is characterized by reticulate cryostructures that reflect shrinking as sediment freezes, a phenomenon most common in fine-grained sediments (French & Shur, 2010). Thaw unconformities occur and are shown by the presence of epigenetic structures bordering diagnostic syngenetic features (French & Shur, 2010). In modern cryostratigraphy, CT scan images have been used successfully to find cryostructures in permafrost from the McMurdo Dry Valleys of Antarctica (Lapalme et al., 2017). However, the small diameter of cores makes the identification of cryostructures difficult due to their scale-dependence (Gilbert et al., 2016).

3 Methods

The Camp Century sediments are well preserved and minimally if at all deformed despite their spending at least hundreds of thousands of years buried under almost a mile of ice. Because of the high level of preservation, we employed standard geologic practices to study the stratigraphy and mineralogy of the sub-glacial materials. We used frozen samples for μCT, and after thawing at 4°C, we used bulk sediment for XRD and SEM analysis on a total of 26 samples from the archive. For the μCT analysis, we used two subsamples per core section (subsequently referred to as (a) and (b)), for a total of 49 subsample scans. Bierman et al. (2024) describe the core cutting and allocation procedure in detail.

With the fundamental core stratigraphy now defined (Bierman et al., 2024) and prior work suggesting the composition of rocks in the core (Fountain et al., 1981) as well as the presence of fossil material and the timing of interglacial exposure

180   (Christ et al., 2021, 2023; Harwood, 1986; Whalley & Langway, 1980), the goal of this paper is to understand and document better the mineralogy of the sediment, the sedimentary and cryostructures that characterize the material, and the sequence of events recorded in the sub-glacial material.

3.1 Micro-Computed Tomography

    We created a digital archive of the (a) and (b) sub-samples, 49 in total, by collecting a series of µCT scans. We
185   scanned sub-samples (a) and (b) from each core section using a Bruker SkyScan1173 µCT scanner fit for use in a cold room at -10°C at the Cold Regions Research and Engineering Laboratory (CRREL) in Hanover, NH. Each of the ~10 cm-tall samples were scanned in two overlapping 7.9 cm-tall sections at a resolution of 71 µm/voxel to capture the entire length of the sample. We completed reconstructions for each scan using the Bruker NRecon software. This resulted in 84 partial sample scans, 7 full sample scans, and 8 zoomed scans. Two scans resulted in failed reconstructions due to difficulty with the scanning procedure.
190   The raw data are archived with the Arctic Data Center (Perdrial et al., 2024). 3D visualization of all scanned samples are available for viewing and download at this online, public repository: https://www.morphosource.org/concern/cultural_heritage_objects/000583438.

    Qualitative assessment and 3D visualization of the partial scans, using Bruker's CTVox software, allowed us to investigate contacts, layering, sorting, lineations, and permafrost features of each sample. The 3D nature of the CT scans allows
195   us to look at internal structures by slicing into the models laterally. We also were able to filter the intensity of the beam response to only display the denser suspended particles to look for other structures such as layering and particle alignment. The angularity of larger grains was also assessed visually with a classification scheme that defines grains having sharp edges as angular and grains with smooth, curved sides as rounded, and a range of intermediate shapes (Janoo, 1998).

3.2 X-ray Diffraction

200   We analyzed the crystalline composition of selected core samples by XRD using a Rigaku MiniFlex II, equipped with a Cu X-ray tube. Following qualitative diffractogram analysis, we quantified the diffractograms using the Rietveld Full Pattern Profile Fit algorithm included in the PDXL-2 software (PDXL, Rigaku Corp). Our analysis used a representative group of 15 samples from various sections of the sub-glacial core (Table 1). We used approximately 0.2 g of bulk sediment from each sample and ground it manually with a mortar and pestle. The ground sediment was mounted on a zero-background plate in
205   random orientation mounts and analyzed in 2theta-theta geometry between 3 and 70 °2θ with a dwell time of 1 degree/min and 0.02 °2θ resolution for a total run time of 67-minutes. We characterized the mineralogy using databases from the International Center for Diffraction Data 2.0 and Crystallography Open Database for peak matching. Subsequently, we performed quantitative analysis of the X-ray diffractograms using a semi-automatic Rietveld approach (Rietveld, 1969). To refine our results, we varied the values for scale factor, cell parameters (within 0.2Å), shape parameters, and for selected minerals (clays
210   and amphiboles), the March–Dollase preferred orientation parameter, similarly to the method described in Mackowiak and Perdrial (2023)). Untreated diffractograms are archived with the Arctic Data Center (Perdrial et al., 2024).

3.3 Scanning Electron Microscopy Imaging and Energy Dispersive X-ray Micro-mapping

We performed two different types of SEM analyses: SEM imaging and elemental mapping of polished mineral surfaces and SEM high resolution microphotography of grain textures and shapes (Table 1). Using the first approach, we collected imagery of the polished grains at a high resolution. We embedded thawed bulk sediments in epoxy resin (EPO-TEK 301). After curing for at least 24 hours, we micro-polished the resulting epoxy puck using a decreasing grit size to 0.05 μm. The mounts were carbon sputter-coated prior to analysis in backscattered electron (BSE) mode using a TESCAN VEGA3 scanning electron microscope coupled with an Oxford Instruments Aztec Elemental Mapping Energy Dispersive X-ray Spectrometer (EDS) in the Geology Department at Middlebury College (Vermont, USA). We acquired BSE images and EDS maps at 20 keV for a minimum of 20 frames totaling 10-minute elapsed time for each multi-elemental map. Then, we generated multi and tri-color maps using the Gatan digital micrograph 3.1 software. We imaged 15 samples with the SEM and analyzed 2 sites on each mount (except sample 1059-6 which was imaged only at one site) resulting in 29 individual images archived with the Arctic Data Center (Perdrial et al., 2024).

We conducted grain coating evaluation over all 29 images. To do so, we used the EDS maps to evaluate each grain and placed it, based on our visual assessment of grain coating abundance, into the following five unique categories: grains dominated by coating (>50% coverage), grains with moderate coating (<50% and >25% coverage), grains with little to no coating (<25% coating), grains with coating only in cracks, and fine particle aggregates. Observations from two sites of the same samples were merged so that there is one summed evaluation per sample and 5 samples were counted by two different observers to ensure consistency. Counts were converted to percentages to normalize data between samples. We created the category "High Abundance" which includes the dominated and moderately covered by coating categories to communicate abundance vs. depth more succinctly.

At the Geological Survey of Denmark and Greenland, we acquired another set of SEM images in BSE at a lower resolution for grain size and shape analysis of all mineral compositions. Images at the lower magnification were collected for 9 samples throughout the core. The 9 samples were mounted in epoxy and coated with 10 nm carbon to make them conductive. Backscattered electron contrast (BSE) images were generated at the ZEISS Sigma 300 VP equipped with a field emission gun, using the ZEISS Mineralogic™ software platform. A mosaic of BSE frames of a representative part of the sample was taken. Further details on the software and applied method can be found in Keulen et al. (2020). Analyses were performed with acceleration voltages of 15keV using a 120 μm^2 aperture.

We analyzed unpolished grains from the 125 to 800 μm fractions in secondary electron mode at high resolution with SEM to observe grain microtextures. This was done at the Service Commun de Microscopie Électronique et de Microanalyse X (GeoResources, Nancy, France) using a JEOL 7600F with a 1 nA primary beam operating at 15 keV. Before collecting SEM images, grains were rinsed in milliQ water. They were dried and attached to adhesive paper before carbon coating. We used these high-resolution images to examine textural features at the grain surface (e.g., Cailleux & Tricart, 1959; Mahaney, 2002). We analyzed 9 samples (see Table 1) and report here the key observations.

245 **Table 1. Summary of samples and physical, geochemical, and mineralogic analyses performed. Asterisks denote samples analyzed in work performed and reported by Christ et al. (2021).**

			SEM imaging			
Sample[a]	Depth (cm)	XRD	BSE, low mag[b]	BSE, high mag[c]	SE, high mag[d]	μCT
1059-4	0-10	*	*	*	Analyzed	Not scanned
1059-5	10-20	Analyzed	Not run	Analyzed	Not run	Scanned
1059-6	20-29.5	Analyzed	Analyzed	Analyzed	Analyzed	Scanned
1059-7	29.5-34	Analyzed	Not run	Analyzed	Not run	Scanned
1060-A1	34-44.5	Not run	Analyzed	Not run	Analyzed	Scanned
1060-A2	44.5-55.5	Analyzed	Not run	Analyzed	Not run	Scanned
1060-B	55.5-78.5	Analyzed	Analyzed	Analyzed	Not run	Not scanned
1060-C1	78.5-88.5	Analyzed	Analyzed	Analyzed	Analyzed	Scanned
1060-C2	88.5-98.5	Analyzed	Not run	Analyzed	Not run	Scanned
1060-C3	98.5-108.5	Not run	Analyzed	Not run	Analyzed	Scanned
1060-C4	108.5-118	Not run	Not run	Analyzed	Not run	Scanned
1060-C5	118-129	Not run	Not run	Not run	Not run	Scanned
1061-A	129-137	Analyzed	Not run	Not run	Not run	Scanned
1061-B	137-159	Analyzed	Not run	Analyzed	Not run	Not scanned
1061-C	159-171	Not run	Analyzed	Not run	Not run	Scanned
1061-D1	171-181	Not run	Not run	Not run	Not run	Scanned
1061-D2	181-191	Analyzed	Not run	Not run	Not run	Scanned
1061-D3	191-201	Not run	Analyzed	Analyzed	Analyzed	Scanned
1061-D4	201-215	Missing	Missing	Missing	Missing	Missing
1061-D5	215-223	Analyzed	Not run	Analyzed	Analyzed	Scanned
1062-1	223-231	Analyzed	Not run	Analyzed	Not run	Scanned
1062-2	231-238	Not run	Not run	Not run	Not run	Scanned
1062-3	238-250	Analyzed	Not run	Analyzed	Not run	Scanned
1062-4	250-263	Not run	Analyzed	Not run	Not run	Scanned
1063-1	263-273	Not run	Not run	Not run	Not run	Scanned
1063-2	273-283	Analyzed	Not run	Analyzed	Analyzed	Scanned
1063-3	283-294.5	Missing	Missing	Missing	Missing	Missing
1063-4	294.5-305.5	Not run	Not run	Not run	Not run	Scanned
1063-5	305.5-317	Not run	Not run	Not run	Not run	Scanned
1063-6	317-327	Analyzed	Analyzed	Analyzed	Not run	Scanned
1063-7	327-337	*	*	*	Analyzed	Not scanned

280

[a] Sample names notation described in (Bierman et al., 2024)

[b] BSE, low mag denotes samples analyzed in backscattered mode on polished mount, used for the morphology analysis on all particles.

[c] BSE, high mag denotes samples analyzed in backscattered mode on polished mount used in coating estimates, PCA and K-mean clustering.

285 [d] SE, high mag denotes samples analyzed in secondary electron mode used for grain texture analysis.

3.4 Image Analysis

We postprocessed the EDS images of high magnification polished grain data to determine grain size and grain shape parameters of quartz grains only to remove the influence of coating and clays or polycrystalline grains using Fiji (Schindelin et al., 2012; Vandel et al., 2020). To isolate quartz grains, we used multielement color maps created with Gatan's Digital

290   Micrograph and we performed a color threshold to select the Si-O only phases (quartz). We then performed particle analysis on the Fiji platform. We measured three grain size/shape parameters (area, roundness, and circularity) and stored the average and standard deviation for each parameter. Fiji calculates circularity as $4\pi(Area/Perimeter^2)$, which returns values between 0-1, where a value of 1.0 indicates a perfect circle. Roundness is calculated as $4*Area/(\pi*major\ axis^2)$, which returns values between 0-1, where larger values indicate increasing roundness.

295   We performed another image analysis on the set of SEM images acquired at a low magnification, allowing for a larger dataset. For this analysis, we included all grain compositions. The parameters grain size, circularity and roundness were measured using particle analysis in Fiji and a Tukey-Kramer honestly significant difference (HSD) pair-wise comparison was performed on the means for each sample in JMP Pro 15.0.0 (*JMP*, 2024). In all cases the significance level (α) was set at 5%. To represent significance between classes, we report differences using connecting letters where levels not connected by the

300   same letter are significantly different.

## 3.5 PCA Analysis and K-means Clustering

Methods for reducing the dimensionality of a dataset, including principal component analysis (PCA) and K-means clustering, can be useful when interpreting physical grain characteristics and geochemical aspects (Jansson et al., 2022). To assess our unit assignments, we performed a PCA analysis and K-means clustering on data from our quantitative image analysis

305   of quartz grains. The size and shape parameters (including standard deviations) from the image analysis, combined with percent ice composition, percent fine-grained fraction composition, percent quartz composition, depth, and an ordinal evaluation of grain coatings varying from 0-2 (no coating, minimal coatings, and extensive coatings; determined visually) were used as input variables in a K-means clustering method. The data set includes the 11 variables mentioned above, measured over a total of 29 observations from the 15 samples. The cluster centers were calculated using a "nearest centroid sorting" approach

310   (Anderberg, 1973; *JMP*, 2024). We performed a PCA to create a new set of uncorrelated variables to help reduce the noise in our data, and then performed a K-means clustering in JMP Pro 15 to assess the optimal number of clusters according to the cubic clustering criterion. Z-scores, which normalize our input variables based on the feature mean and standard deviation, were calculated in R (R Core Team, 2022).

4 Results

Our multiscale analysis supports, refines, updates, and provides more justification and detail regarding unit delineations proposed earlier (Bierman et al., 2024; Christ et al., 2021, 2023; Fountain et al., 1981). Size distribution shows at least 16% abundance of very fine sand and silt-sized grains in all units (in some units the abundance of fines is over 90%) and more variability in size in the lower part of the core. The percent abundance of grain coatings increase with depth and coatings are largely absent in the upper two units (4 and 5). Grain shape analysis (roundness and circularity) does not vary systematically within or between units. PCA and subsequent K-means analysis quantitatively corroborate our understandings of these systems. Grain microtextures show that grains in the sub-glacial material record different histories.

4.1 Micro-Computed Tomography
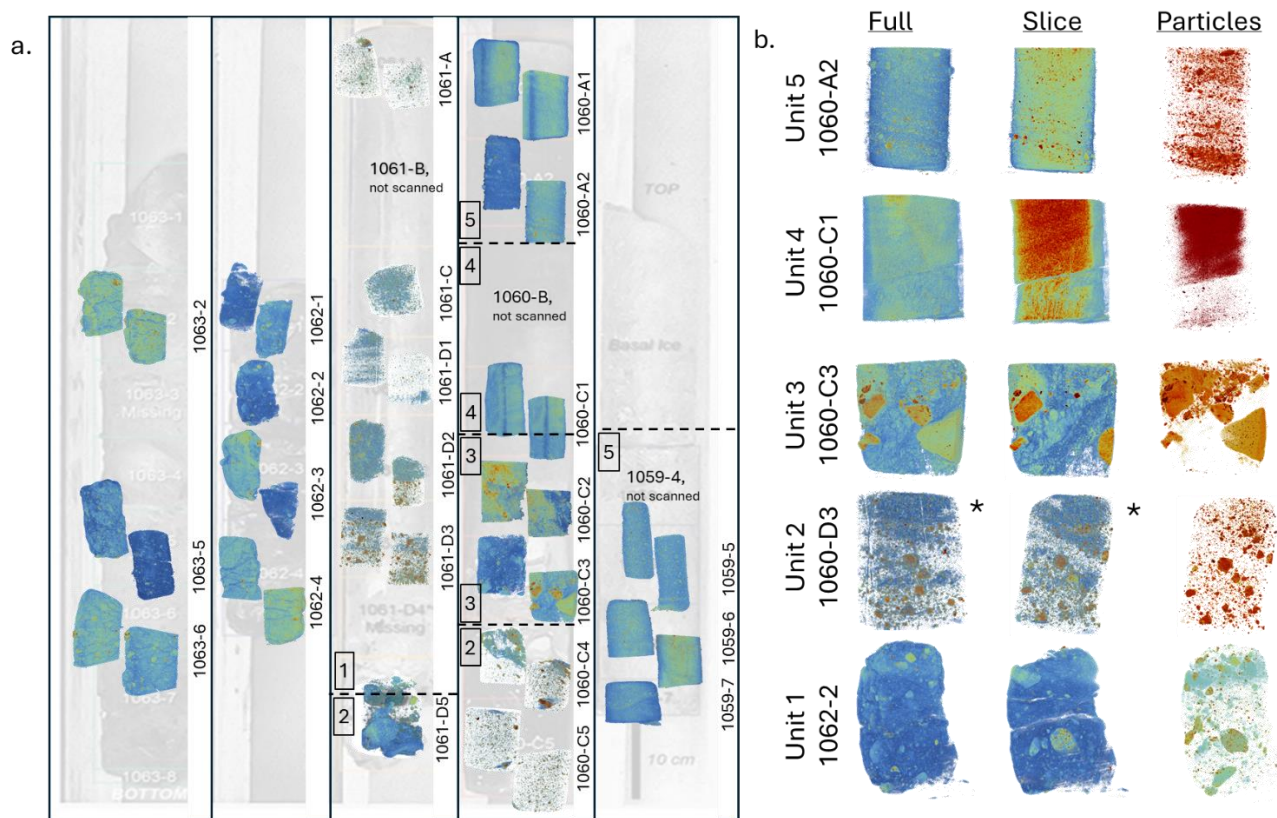
Figure 2. (a) CT scans layered over historical image of original core (Fountain et al., 1981). Scans were acquired in overlapping sections, each individual scan is ~8 cm tall. Samples not scanned are noted and missing samples from the archive are shown as gaps. Dashed horizontal lines denote unit delineations and are noted by unit number. (b) Selected representative samples per unit. Samples 1060-A2, 1060-C1, 1060-C3, and 1062-2 are shown with three views, a full view, an internal slice, and a filtered view of just the dense suspended particles. The first two examples of 1060-D3, marked by an asterisk, show different angles of the sample to show the vertical clear ice inclusions and strong banding. Note that the orientation between samples is not known as no note of the core orientation exists in the archive.

11

MicroCT scans show that the lowermost 7 samples define a homogeneous unit (Unit 1; 223-327 cm depth below the ice-sediment interface) – a diamicton displaying a variety of cryostructures (Fig. 2a). These 7 samples are characterized by

335   variably sized clasts (ranging from angular to sub-rounded and spherical to elongated) in a finer matrix with no bedding. Throughout the unit, sub-horizontal ice lenses cut through the sediment in a braided lenticular pattern (see example in 1062-2, Fig. 2b). At the top of the Unit 1 diamicton, the CT scan of sample 1061-D5 (215-223 cm) captures a transition in the type of deposition. The upper part of the sample has a high ice content compared to the lower part of the sample which is sediment-rich like the rest of Unit 1. The transition is not discrete as it consists of 2 ice-rich layers separating the dense fine-grained

340   matrix material of Unit 1. Although no clear difference exists between the sections, the topmost sample (1062-1) appears to have more cryostructures.

    The next 6 samples (1061-D3 to 1060-C4) comprise Unit 2 (108.5-215 cm). They are characterized by low density (<1.2 g/cm^3) and high ice content (>80%) with sediment interspersed throughout. The μCT scans show that sediment is generally fine-grained with few clasts and bedding tilted at approximately a 45° angle from horizontal. The tilted bedding is

345   more apparent in some samples (1060-D3, 1061-D1, and 1060-C4). Vertical fractures filled with clear ice create intersecting planes in the sediment-laden ice. The contact at the top of the unit (1060-C1) is angled and intermixed with the unit above, similar to the contact with the lower sediment.

    MicroCT scans of samples in Unit 3 (88.5-108.5 cm) show deformed bedding, normal grading, and some reticulate cryostructures. The samples in this unit are 1060-C3, 1060-C2, and the lower portion of 1060-C1. In 1060-C3, there is no

350   visible bedding, instead the sample contains pebble-sized clasts in a silt-sized matrix with lower ice content (23%) (Bierman et al., 2024). Clasts angularity ranges from sub-angular to sub-rounded. Cryostructures in the silty matrix form a reticulate pattern in sample 1060-C3. Sample 1060-C2 and the lower portion of 1060-C1 are characterized by the presence of a deformed fine-grained bedding with high ice content (49%) (Bierman et al., 2024). There is a very distinct unconformable contact in sample 1060-C1 (at an angle of 11°) with the upper sediments, distinguishable by μCT scans (this contact is more apparent in

355   subsample (b) whereas in subsample (a) the contact is less distinguishable) (Fig. 2b). Directly below the contact bedding curves from sub-horizontal, downward to nearly 90° which continues into 1060-C2.

    Both units above Unit 3 are similar in structure, containing well-sorted bedded sand. Unit 4 (55.5-88.5 cm) includes sample 1060-C1 (the part above the contact) and 1060-B (not scanned). These sediments are bedded, well sorted, fine-grained sand. Bedding in these samples is distinct, parallel, and sub-horizontal with a ~15° dip. The well-sorted fine-grained nature of

360   the deposit defines this unit.

    Samples 1060-A2 to 1059-5 define Unit 5 (0-55.5 cm). These samples coarsen upward into gravelly sand from the fine-grained sands of Unit 4. Bedding is well defined in the lower samples in this unit (notably 1060-A2) and becomes harder to distinguish in the top-most sample scanned (1059-5). The layers also dip at 15°. There are some small pebble-sized clasts, which range from sub-rounded to sub-angular, that form individual beds. Well-sorted sand-sized grains that coarsen upward

365   with well-formed bedding define the upper most part of the core and the top of unit 5 (Fig. 2).
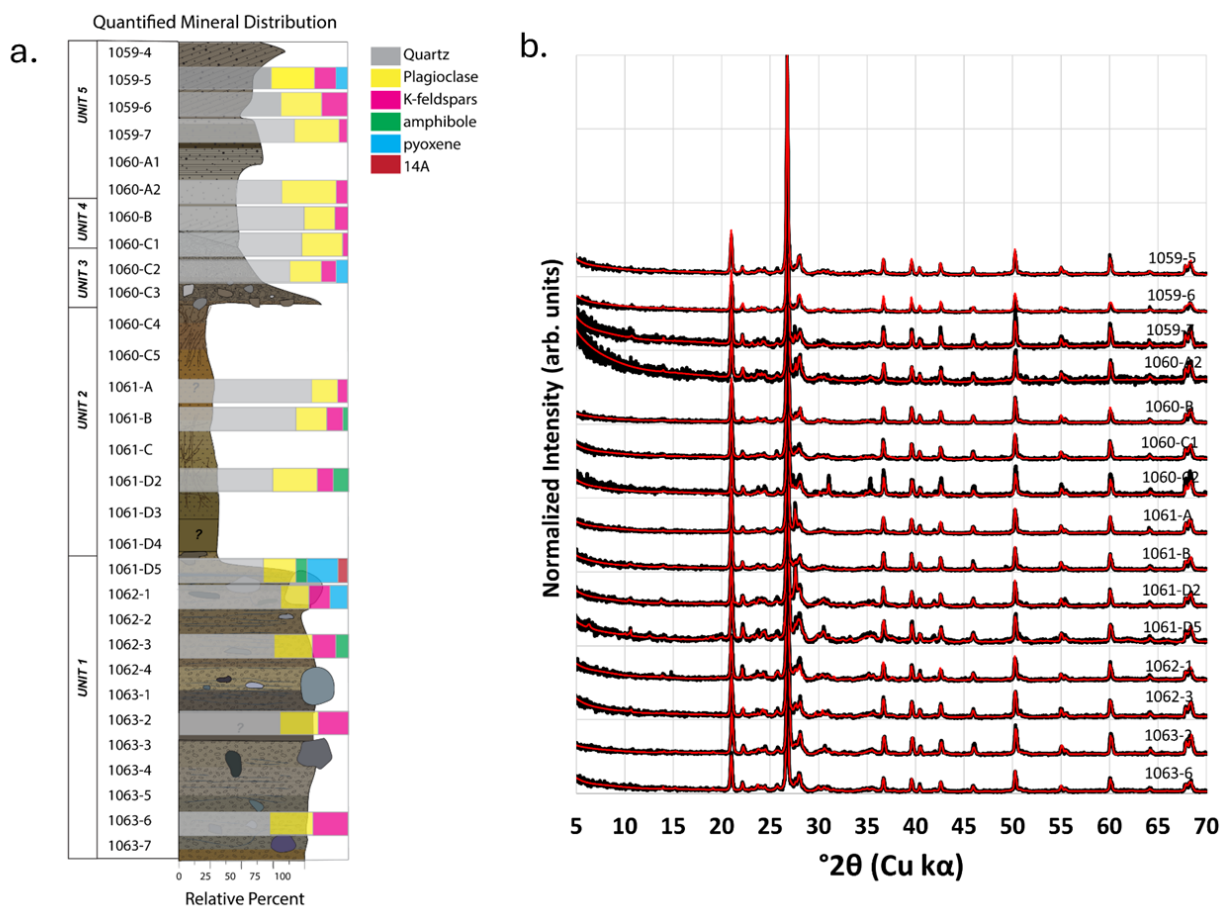
4.2 X-ray Diffraction

Figure 3. (a) Relative mineral assemblage of 15 samples shown with corresponding color bars modeled using the Rietveld method . Stratigraphic column adapted from (Bierman et al., 2024))**. Results are given in Table 2. (b) Diffractograms of all 15 samples measured on the Rigaku MiniFlex II. Modeled diffractograms shown in red were calculated using the Rietveld algorithm included in PDXL-2: Integrated X-ray powder diffraction software.**

XRD analysis indicates little change in relative mineral abundance between units (Fig. 3, Table 2). Throughout the core, the mineralogy is dominated by quartz with lesser amounts of plagioclase and potassium feldspar (Table 2). The average quartz relative abundance is 63.6%±3.9% with a minimum of 49.6% ± 0.7% (1061-D5, Unit 1) and a maximum of 80.6% ± 1.1% (1061-A, Unit 2). We found plagioclase in all units with an average of 22.4% ± 3.5%, with a minimum of 14.8% ± 1.1% (1061-A, Unit 2), and a maximum relative percent of 31.8% ± 1.3% (1060-A2, Unit 5). Potassium feldspar was detected in all samples except 1061-D5 (Unit 1), the average 10.5% ± 3.0% with a minimum of 3.1% ± 0.2% (1060-C1, Unit 4), and a maximum of 19.4% ± 0.8% (1063-6, Unit 1). The relative amount of quartz appears to steadily decrease from the bottom to the top of Unit 5 whereas the relative amount of quartz increases from the bottom to the top of Unit 2. For all other units, the relative proportions of quartz compared to other minerals stays similar.

13

Table 2. XRD quantification (in %) of bulk sediment from select representative samples. Mineralogy reported by mineral group

Sample	Unit	Quartz	Plagioclase[e]	K-feldspar[f]	Amphibole[g]	Pyroxene[h]	Clay[i]	Sum	red. χ^{2j}
				Mineral Content (wt. %)					
1059-5	5	62.2 (1.1)[k]	23.1 (0.8)	14.2 (1.2)	*n.d*[l]	0.4 (0.2)	*n.d.*	99.9 (3.3)	3.5
1059-6	5	56.6 (1.7)	25.3 (1.2)	15.9 (1.7)	2.2 (1.9)	*n.d.*	*n.d.*	100.0 (6.5)	4.8
1059-7	5	70.1 (0.9)	26.0 (0.9)	3.5 (0.2)	0.5 (0.1)	*n.d.*	*n.d.*	100.1 (2.1)	4.4
Unit 5 Average		**63.0 (6.8)**	**24.8 (1.5)**	**11.2 (6.7)**	**1.0 (1.0)**	***n.d.***	***n.d.***		
1060-B	4	75.0 (0.4)	18.4 (0.4)	6.6 (0.3)	*n.d.*	*n.d.*	*n.d.*	100.0 (1.1)	3.8
1060-C1	4	73.7 (0.6)	23.2 (0.6)	3.1 (0.2)	*n.d.*	*n.d.*	*n.d.*	100.0 (1.4)	3.8
Unit 4 Average		**74.4 (0.7)**	**20.8 (2.4)**	**4.9 (1.8)**	***n.d.***	***n.d.***	***n.d.***		
1060-C2	3	66.1 (1.0)	18.3 (1.0)	9.8 (0.6)	*n.d.*	5.7 (0.5)	*n.d.*	99.9 (3.1)	4.7
1061-A	2	80.6 (1.1)	14.8 (1.1)	4.7 (0.3)	*n.d.*	*n.d.*	*n.d.*	100.1 (2.5)	3.5
1061-B	2	68.6 (0.8)	19.9 (0.7)	8.9 (0.5)	2.3 (0.6)	*n.d.*	*n.d.*	99.9 (2.6)	3.5
1061-D2	2	57.3 (1.3)	26.1 (1.5)	9.5 (0.5)	7.0 (0.8)	*n.d.*	*n.d.*	99.9 (4.1)	3.9
Unit 2 Average		**68.9 (11.7)**	**20.3 (5.7)**	**5.8 (2.6)**	**3.1 (3.3)**	***n.d.***	***n.d.***		
1061-D5	1	49.6 (0.7)	20.2 (0.6)	*n.d.*	5.6 (0.5)	19.6 (0.7)	4.9 (0.4)	99.9 (2.9)	3.3
1062-1	1	61.3 (1.3)	17.2 (0.6)	12.0 (1.0)	*n.d.*	9.5 (0.7)	*n.d.*	99.9 (3.6)	4.0
1062-3	1	57.3 (0.8)	22.7 (0.7)	13.9 (0.7)	6.1 (0.5)	*n.d.*	*n.d.*	100 (2.7)	3.6
1063-2	1	60.2 (0.8)	23.4 (0.8)	16.4 (0.8)	*n.d.*	*n.d.*	*n.d.*	100 (2.4)	3.3
1063-6	1	54.3 (0.8)	26.3 (0.8)	19.4 (0.8)	*n.d.*	*n.d.*	*n.d.*	100 (2.4)	3.0
Unit 1 Average		**56.5 (4.7)**	**22.0 (3.4)**	**12.3 (3.2)**	**5.8 (7.1)**	**2.3 (0.4)**	**1.6 (2.2)**		
1059-4[m]	-	58.6	33.3	4.6	3.5	bql	100		
1063-7	-	61.8	33.8	2.0	2.4	n.d.	100		

[e] Plagioclase includes all plagioclase detected (albite, oligoclase, andesine)

[f] K-feldspar includes all K-feldspar detected (orthoclase, sanidine)

[g] Amphibole includes all amphibole detected (cummingtonite, hornblende, ferrosilite)

[h] Pyroxene includes all pyroxene detected (pigeonite)

[i] Clay includes micas, kaolinite and chlorite-like phases

[j] red. χ^2 represents the goodness of fit and correspond to $\chi^2 = [\Sigma_i (I_{obs} - I_{calc})_i^2 / \sigma^2(I_{obs})_i] / (n - p)$; with I the intensity, $\sigma(I_{obs})$ the estimated error of the measure (fixed to 10% of the counts), n the number of points used for simulation and p the number of parameters estimated during the fit.

[k] Error in parenthesis is provided by PDXL and represents the standard error for individual phases. For averages, the error is 1SD when n>2 or as deviation from the mean when n=2

[l] n.d. "not detected"

[m] samples analyzed in Christ et al. (2021). Note that plagioclase and K-feldspars were summed as feldspar, no error or goodness of fit was provided. bql stands for below quantification limit as clay minerals were detected in 1059-4 but not quantified.

4.3 Scanning Electron Microscopy Imaging and Energy Dispersive X-ray Micro-mapping
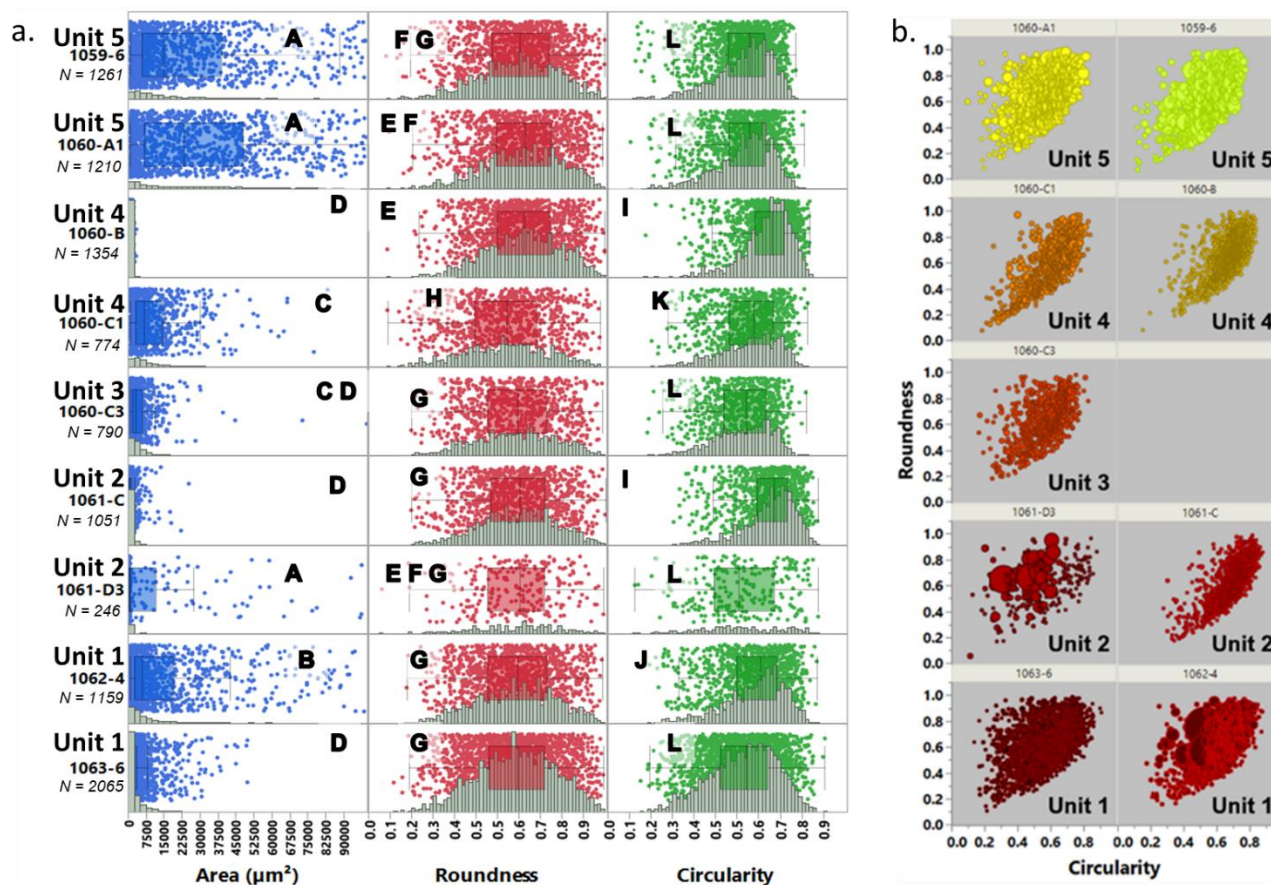
Figure 4. Grain size and shape parameters extracted from low magnification SEM backscattered images of selected core samples. (a) Distribution of grain size (area), roundness, and circularity for individual samples, N is number of particles examined. For simplification, the maximum area displayed is limited to 100,000 um². Roundness and circularity parameters were defined in section 3.4. The letters refer to the pairwise significance of means (described in 3.4). Samples assigned the same letters do not show a significant difference, samples that do not share the same letter are significantly different. (b) Relationship between particle size, circularity, and roundness for selected individual samples. The size of each individual circle represents the relative area of individual grains.

Fine-grained particles (section area <2500 µm²) in plan-view (corresponding to a 60 µm circular equivalent diameter) are present in all samples, though the range of grain sizes differs per sample (Fig. 4a). Samples 1060-B and 1061-C contain 99.3% to 90.3% of particles with an area less than 2500 µm², respectively. Samples 1059-6, 1060-C3, 1061-D3, and 1063-6 have on average 58% ± 64% fines (area <2500 µm²) and 1060-A1, 1060-C1, and 1062-4 have an average of 19.5% ± 2.3% fines. Samples 1059-6, 1060-A1, and 1062-4 show a much wider distribution of grain sizes (Fig. 4a). Pair-wise statistical analysis of grain size distribution finds three sample groups: 1059-6, 1060-A1 and 1061-D3, sample group 1060-B, 1061-C and 1063-6, and sample 1062-4 as different from each other by particle size.

Roundness has a mean value of 0.62 ± 0.01 with a maximum value of 0.65±0.005 (1060-B) and minimum of 0.58±0.006 (1060-C1), indicative of moderate roundness. While all distributions of roundness are symmetric and unimodal, a Tukey-Kramer mean comparison tests shows that the grains in sample 1060-C1 are significantly different from those in other samples and that the grains in sample 1060-B are also significantly different from those in 6 of the 9 samples (Fig. 4).
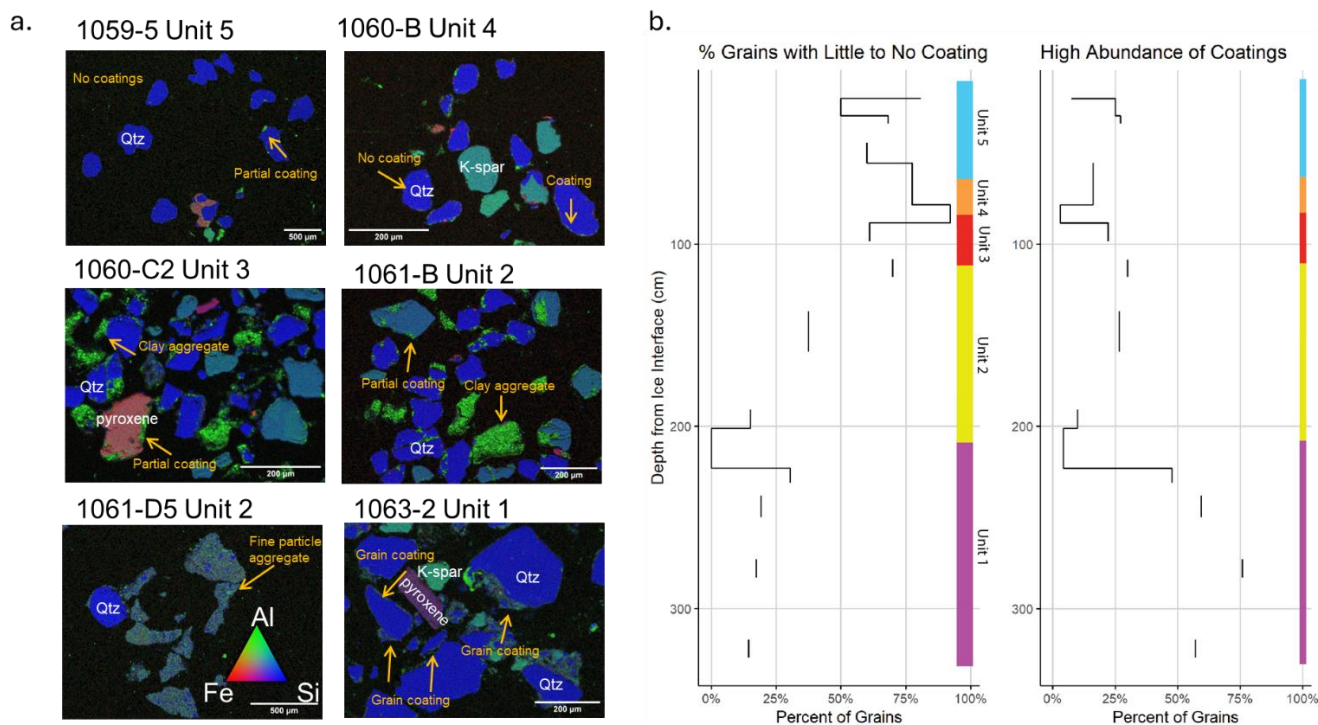
Figure 5. (A) Scanning electron microscopy images showing mineral type and observed coatings. Blue color indicates high silicon content (quartz); green is associated with aluminum (clays and feldspars), and red is associated with iron. **(B)** Abundance of grain coatings down core showing percentage of grains with little to no coating and percent of grains with a high abundance of coatings (dominated and moderate categories combined). Colored bar shows unit assignments with depth.

Circularity is consistently left-skewed and biased towards higher circularity values; all samples fail the Anderson-Darling test for normality. A Tukey-Kramer test splits the data into four distinct groups: (I) 1060-B and 1061-C, (J) 1062-4, (K) 1060-C1, and (L) 1059-6, 1060-A1, 1060-C3, 1061-D3, and 1063-6. These groups separate similarly to the grain size distribution except for sample 1060-C3. Comparing size, roundness, and circularity, larger grains tend to have a lower circularity and higher roundness (based on a significant negative and positive Pearson coefficient, respectively) (Fig. 4b).

Elemental mapping analysis of SEM images by EDS reveals strong patterns between grain coatings and core depth. Grain coatings and fine particle aggregates are most abundant in Unit 1 and are present in all Unit 1 samples (Fig. 5a, b) where they appear to be composed of either individual clay minerals (Al-rich) or fine polymineralic fine aggregates (Si- and Al-rich). Unit 2 has a mix of fine particle aggregates, grain coatings, and clay aggregates, but not all grains have coatings and others are

16

partially coated (Fig. 5a). In this unit the coatings and aggregates are dominated by Al-rich clay-like minerals. Unit 3 has clay
455   aggregates and grains that are partially coated (Fig. 5a). Units 4 and 5 have fewer grain coatings than the other units.

Elemental mapping using principal constituents Si, Fe, and Al allows us to identify quartz (high Si), feldspar and clay
(high Al), and Ca-Fe-Mg rich pyroxene and amphibole (high Fe) (Fig. 5a). Quartz and feldspar, including plagioclase,
dominate all samples. There is a positive correlation (correlation coefficient, 0.7) between the "high abundance" grain coating
category (grains with more than 25% of grain coating around their perimeter) and core depth (Fig. 5b). Tukey-Kramer
460   comparison by "high abundance" and unit reveals that Unit 1 is different from all other units and that Unit 3 has similarities
with Unit 1 and all other units.

Grain surfaces display a variety of micro-textures. High-resolution SEM morphometric imagery of individual grains
reveals that most quartz and feldspar grains have a variety of shapes, with two main endmembers: fresh angular grains with
high relief, and round and oblong grains. Some grains have shapes intermediate between these endmembers (Fig. 6). Round
465   and nearly round grains are rarely pristine and display superimposition of different textures. We find that a considerable number
of grains display high relief features including deep troughs, sharp angles, conchoidal fractures, and adhering particles (Fig. 6
B: 1059-4, E: 1059-6, H: 1063-7). Some grains show V-shape percussion cracks (Fig. 6 A: 1059-4, G: 1063-7) and a few
grains display bulbous edges (Fig. 6 D: 1059-4). Many grains display dissolution pits (Fig. 6 F 1060-C3), multi-micron-thick
coatings containing K and Fe (Fig. 6 G: 1063-7, H: 1063-7), and quartz overgrowth (Fig. 6 A: 1059-4, F: 1060-C3). We found
470   that grains within the core were homogeneous in terms of shape and texture, except for samples from Unit 1 that displayed
more abundant weathering features than other units, in agreement with other SEM observations from polished grains (Fig. 5).

17
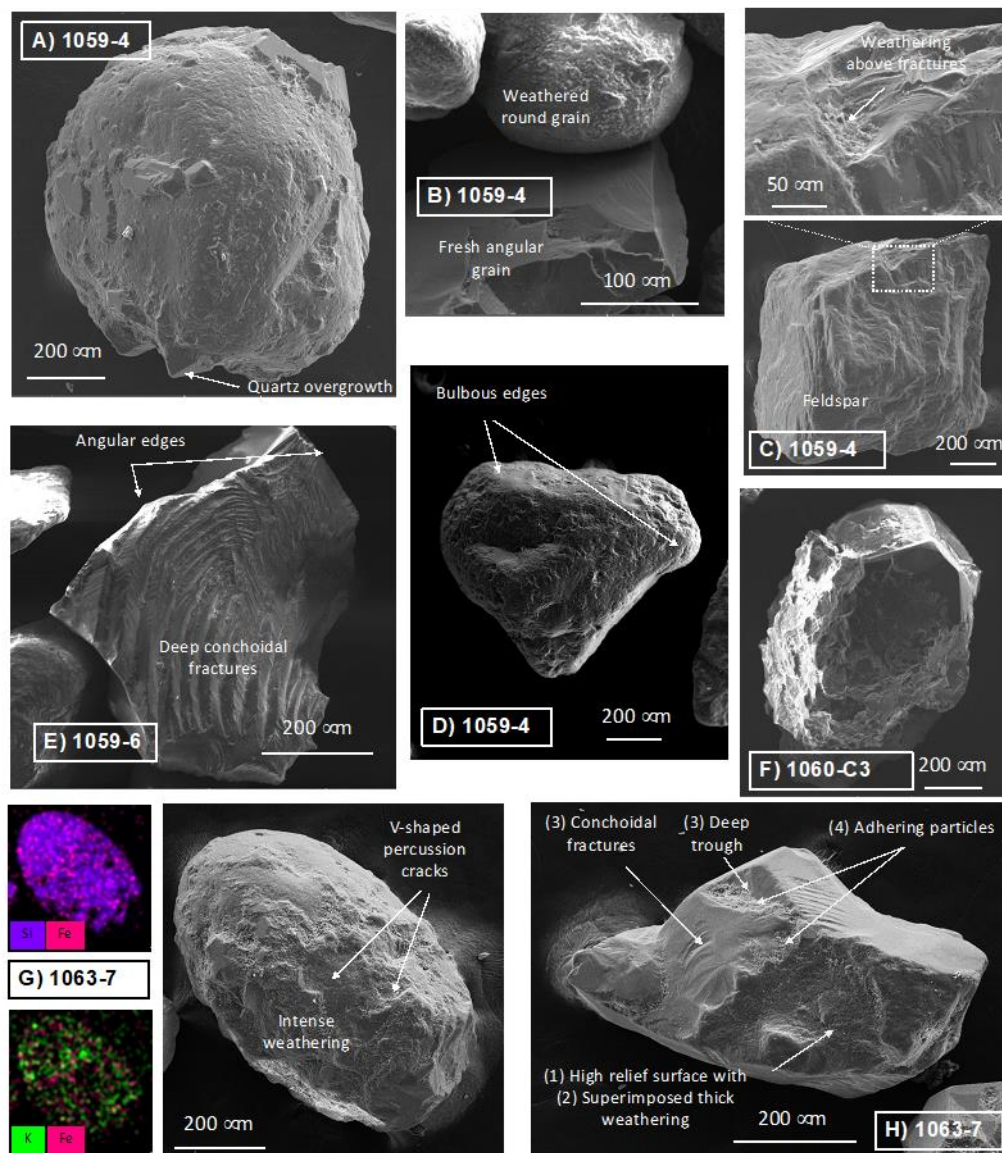
Figure 6. SEM imagery from samples of Camp Century grains. A) 1059-4: round quartz grain with deep grooves, V-shape percussion cracks and quartz overgrowth, B) 1059-4: upper grain is rounded quartz with significant weathering and solution pits. Lower grain is a fresh angular quartz grain, with features consistent with glacial crushing and adhered fine-grained particles. C) 1059-4: K-feldspar angular grain with weathered surfaces. Top detail shows weathering features superimposed on preexisting fresh fractures. D) 1059-4: Subangular quartz grain with percussion marks and bulbous edges. E) 1059-6: Angular quartz grain with deep conchoidal fractures. F) 1060-C3: subrounded quartz grain with weathering dissolution features and quartz overgrowths, G) 1063-7: oblong quartz grain with remnant V-shaped cracks, significant weathering/coating features, and fresher surfaces. Backscattered electron analysis shows the presence of Fe and K in the thick micrometric coating. H) 1063-7: angular quartz grain with 1) an initial high relief surface affected by 2) a thick weathering rind, then later 3) deep trough and conchoidal fractures covered by 4) adhering particles.

18

4.4 PCA and K-means Clustering

485   K-means clustering analysis shows optimal clustering occurs with 5 clusters (Fig. 7a, b). There are similarities with this clustering and our unit assignments, notably Unit 1 samples are clustered tightly together. There is mixing of Units 3, 4, and 5 samples across Clusters B and C. Unit 2 has samples within 3 different Clusters A, B, and D (Fig. 7b).
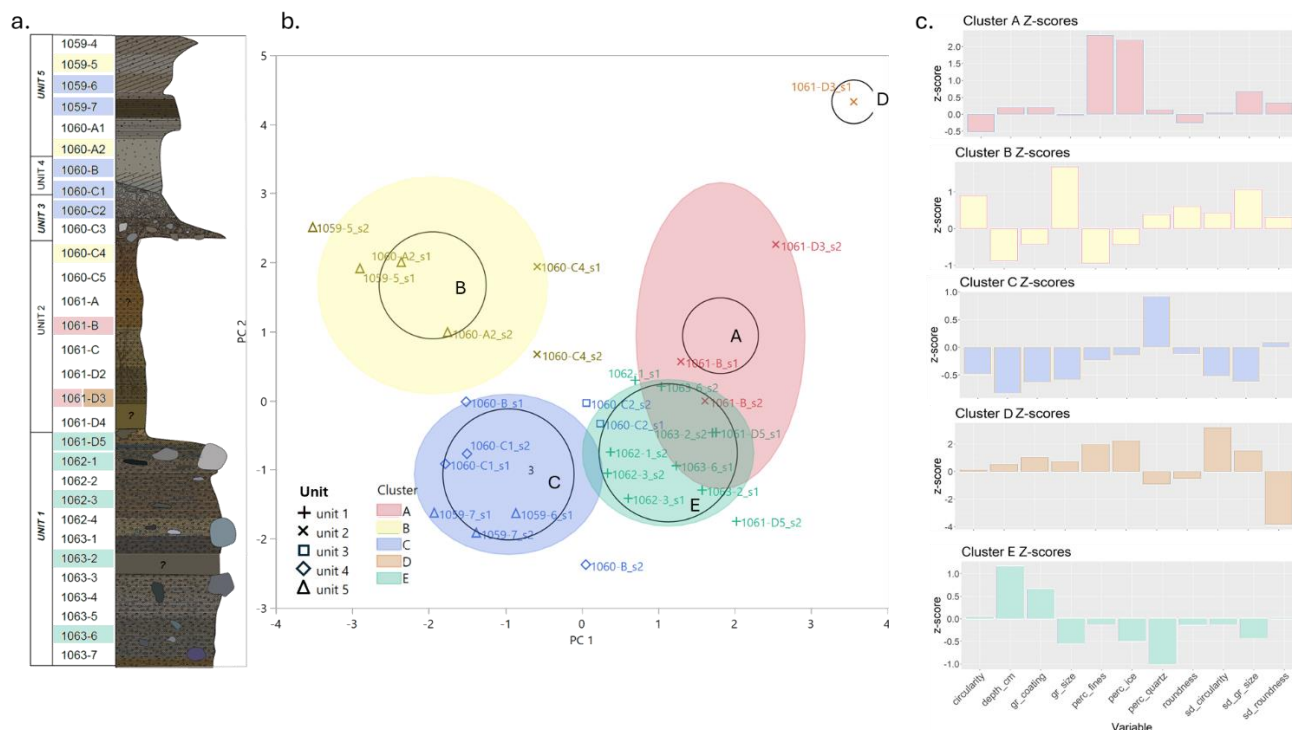
Figure 7. (a) Stratigraphic column with samples highlighted according to the K-means custering (b) K-means clustering analysis on
490   multiscale physical, mineralogical and geochemical data. The data are plotted showing the first two principal components (PC 1 and 2), and are categorized into 5 clusters; clusters are color-coded and assigned a letter. Unit assignments are indicated by shape. (c) Z-scores of each cluster are shown, which indicate how many standard deviations (y-axis) the mean of each variable in the cluster differs from the observed mean across all data. All Z-score graphs have the same x-axis variables in the same order as shown in the Cluster E graph.

495   Significant variables associated with PC1 include depth, percent quartz, grain coating, and percent fines. This principal component can be summarized as relating to transport processes, as percent fines and percent quartz often reflect sorting that occurs during transport and grain coatings are stripped in part or entirely during transport processes. Significant variables associated with PC2 are grain size, standard deviation of grain size, standard deviation of circularity, and circularity to a lesser extent. This component represents aspects of grain morphology. According to PC1, transport process, there is a
500   larger separation between Clusters A and B than there is between E and C (Fig. 7b). Along PC2, clusters A and B are separated from Cluster C and E. Cluster D contains one sample belonging to Unit 2 (1061-D3) and it is positioned at extreme ends of both principal components showing there is a strong difference between this sample and the rest of the data. The other

observation associated with sample 1061-D3 (as two images were analyzed for this sample) is assigned to Cluster A but is positioned at high ends of both axes, as is the same for Cluster D.

505   The Z-scores help us interpret which variables are driving (responsible for placing) samples into a particular cluster and provide insight into why there may be disagreements between our unit assignments and the clusters (Fig. 7b, c). Z-scores for Cluster A, made up of Unit 2 samples, show the most significant factors are percent fines and percent ice with positive Z-scores of 2.3 and 2.2 respectively (indicating the number of standard deviations that values for these variables are from the population mean in this cluster, comparatively) (Fig. 7c). This means Cluster A samples (Unit 2) have more fine-grained

510   particles and more ice on average than other samples. Cluster B samples (mainly Unit 5) have larger grain size with slightly more size variation and slightly higher values of circularity on average (grain size Z-score=1.7, sd grain size Z-score=1.1, and circularity Z-score=0.9). Samples in Cluster C (Units 3, 4, and 5) can be most succinctly described as having more quartz than samples in other clusters (percent quartz Z-score =0.9). Cluster D (1061-D3, Unit 2) is quite different from the other clusters as it has the largest Z-scores. This sample has low variability in rounding and high variability in circularity with high ice

515   content (sd roundness Z-score =-3.8, sd circularity Z-score =3.2, and percent ice Z-score =2.2). Lastly Cluster E (Unit 1) Z-scores show these samples are at a greater depth and have less quartz on average (depth Z-score =1.2, percent quartz Z-score =-1).

5 Discussion

The rich record of ice sheet history and process we interpret from the Camp Century sub-glacial material indicates

520   that analysis of the material in such cores can provide unique insight into past conditions extending deeper in time than records preserved in the glacial ice above. Expanding paleoenvironmental understanding of Greenland and its ice provides data to understand how both will behave in a warmer future (Gemery & López-Quirós, 2024).

5.1 Sub-glacial Core Stratigraphy: Synthesis of Physical, Chemical, and Mineralogic Observations

The combination of geochemical, mineralogical, and physical data collected from the Camp Century sub-glacial materials

525   across different spatial scales characterizes in detail 5 distinct stratigraphic units building on and refining the work of others (Bierman et al., 2024; Christ et al., 2021, 2023; Harwood, 1986; Whalley & Langway, 1980). From these data, we infer that different surface processes deposited these materials during times when the site was glaciated and when it was not.

Our data demonstrate that after deposition Unit 1 was affected by weathering processes at or near Earth's surface. The unit has abundant grain coatings (Fig. 5b) formed by percolating liquid water most likely during interglacial periods

530   (Marschalek et al., 2024). Warm conditions facilitated the accumulation of grain coatings in the sediment before cooling occurred. After which the formation of permafrost and eventual burial by ice halted grain coating production but maintained the preserved coatings in the sediment. The sub-horizontal, braided, lenticular cryostructures are consistent with syngenetic permafrost formation, suggesting based on cryostratigraphy, little influence of liquid water in Unit 1 after permafrost formation (French & Shur, 2010).

20

535   The high ice content at the top of Unit 3, and cryostructures suggesting epigenetic permafrost formation, imply that the slumping which triggered the deposition of Unit 3 occurred in the presence of liquid water, creating a flow till deposit that later froze (Brevik & Reid, 2000). The mechanism causing slumping is unclear, it could be due to undercutting from a small stream or erosion of permafrost polygons. The normal grading seen in Unit 3 likely resulted from sorting as the sediments flowed downslope, which has been seen in flow till deposits (Brevik & Reid, 2000). The top of Unit 3 differs from the lower

540   part as there is distinct layering and an absence of large clasts. The layering in sample 1060-C2 and under the contact in 1060-C1 could be a marker of multiple flows (Fig. 2b). The lack of coarse clasts in the upper part of Unit 3 may reflect limited flow capacity capable of moving only smaller particles during these later flow events (Brevik & Reid, 2000). The paucity of grain coatings in Unit 3 compared to Unit 1 (Fig. 5), could indicate that the slumping process disrupted grain coatings or mixed sediment from Unit 1 with sediment from the upper units, 4 and 5.

545   Unit 1, glacial till, and Unit 3, a slump deposit, have some similar characteristics in the μCT scans and similar mineralogy (Fig. 2). These similarities are seen in sample 1060-C3, the bottom of Unit 3, which is characterized by variably sized clasts in a fine-grained matrix with no evidence of bedding. The higher ice content and the difference in cryostructures between Units 1 and 3 supports the hypothesis that Unit 3 was deposited in or by liquid water. The presence of Ca-Fe-Mg pyroxene in both units 1 and 3 links them beyond the meso-scale CT observations. Pyroxenes readily weather from sediments (Goldich, 1938)

550   so their inclusion in a sediment with high quartz content could reflect the source rock composition, limited weathering, or mixing with localized sources of different mineralogy. Overall, the similar sedimentary structures and mineralogy suggest that Unit 3 was originally a part of the subglacial till formed below the ice (Unit 1) that was subject to slumping due to saturation of liquid water during interglacial conditions. Micro-texture analysis (Fig. 6) from Unit 1 suggests the same succession of events deduced from meso and macro-observations: initial glaciation and till deposition, then ice-free conditions allowing

555   weathering and the development of grain coatings.

    Unit 2, between Units 1 and 3, marks a stark transition from the sediment-dominated till to an ice matrix with interspersed sediments. The sediment content in Unit 2 and the horizontal alignment of grains in the ice is typical of a basal ice layer (Knight, 1997). The source of the sediment interspersed in the ice is likely the till below (Unit 1) because they share similar mineralogy (presence of pyroxene) and fine particle aggregates, possibly glacial flour (Gresina et al., 2023; Knight,

560   1997). Other possible origins of Unit 2 include interglacial firn or basal ice from a later ice advance, both hypotheses that allow for deep weathering of Unit 1 (Hambreky et al., 1999).

    In Units 4 and 5, there are elevated levels of sorting, minimal grain coatings, and the presence of bedding and contacts indicative of a fluvial depositional environment (Fig. 2). The fluvial system initially transported very fine-grained sand (Unit 4) followed by larger grains representing an increase in system energy (Unit 5). Grain morphology in these units is a mix of

565   round and angular grains, with minimal change from Units 4 to 5 (Fig. 4). Multiple lines of evidence suggest that sediment in Units 4 and 5 was derived from the erosion of Unit 1 (glacial till) and transported by moving water. Grain textures shown in SEM imagery (Fig. 6) show that Units 4 and 5 contain many grains with fresh surfaces, glacial crushing features, and sharp

angles. This suggests that that they originate from a proximal source of glacial sediment, and were not transported over a long distance, probably over a less than few km long watershed (Mahaney, 2002).

570   Most of the more rounded grains in Units 4 and 5 display significant weathering features and glacial crushing, implying that their oblong and round shapes were probably inherited from previous ice-free cycles (pre-Pleistocene sandstone deposits are observed in northern Greenland (Gregersen et al., 2022)). Hence, neither the increase in system energy nor fluvial transport influenced grain rounding (Kuenen, 1959). Unique to Units 4 and 5, are grains with coatings only in cracks or concave structures that protected the coatings from abrasion during transport, preserving evidence of past weathering (Fig. 5). This

575   implies that these sediments originally had more substantial grain coatings that were stripped during fluvial transport – consistent with geochronologic data showing that minerals in Unit 1 and Unit 5 have similar cooling ages (Christ et al., 2023).

The paucity of the heavy minerals in the fluvial sediments could reflect hydraulic sorting, with the result that denser minerals, including pyroxene and amphibole, are deposited with larger grain size fractions (Malusà et al., 2016). This would explain the lack of heavy minerals in the finer grain size fraction (Unit 4) and the presence of pyroxene at the top of Unit 5

580   where coarser grain sizes are included, brought in by a flow with the capacity to carry larger and denser grains (Garzanti, 2017; Malusà et al., 2016).

Statistical analysis (PCA and K-means, Fig. 7) clearly separates materials based on glacial and non-glacial origin. PC1, relating to transport processes, separates the data between glacially influenced Units 1 and 2 and fluvially driven processes characteristic of Units 3, 4, and 5. Unit 3 samples overlap with Cluster E (Unit 1) which supports our interpretation that these two units both originate from the same glacial till. PC2, relating to grain morphology, does not show any distinct

585   trends relating to our unit assignments (Fig. 7). The grain morphology analysis shows a similar complexity (Fig. 4) which indicates intra-unit variability not seen on the meso or macro-scale.

Amongst all the units, Unit 2 is the most scattered across the PCA which could be an indication of a more complex history of formation. The SEM data for Unit 2 echoes this complexity as it has the most intra-unit variability. Despite the

590   variation within the unit, some of the samples closely resemble other units at the micro-scale. Sample 1060-C4, at the top of Unit 2, is most reminiscent of an upper fluvial sample (Unit 5) as it has minimal grain coating and above-average grain size (Fig. 6c). Conversely, sample 1061-B, near the middle of Unit 2, has aluminum-rich clay coatings which are also present in samples from Unit 3. On the PCA, 1061-B samples are situated near Unit 1 and 3 samples, corroborating the similarities seen at the micro-scale. Samples closer to the contact with Unit 1 (1061-D3) are characterized by small particle aggregates that are

595   unique to this section of core. The 1061-D3 samples plot at the high end of PC 1 and 2 emphasizing their distinction from other parts of the core (Fig. 7b).

The spread of data from Unit 2 could be an indication of environmental changes represented by this ice unit or of mixing between units above and below (Units 1 and 3). For example, we have characterized Units 5 and 3 as having quite different transport mechanisms and diagnostic characteristics of both these units are present in Unit 2. The inclusion of particles

600   with characteristics like those in other units could imply that the changes seen throughout Unit 2 indicate variability in the mechanism of particle inclusion in the ice.

5.2 Proposed Sequence of Environmental Changes at Camp Century

The Camp Century sub-glacial materials preserve a sedimentary record of changing surface and subglacial processes. From our multi-scale investigation of these materials, we present a plausible sequence of ice retreat and advance events consistent with evidence including documented surface exposure during MIS 11 (Fig. 8) (Christ et al., 2023).

1. *Initial conditions*: The bottom part of the core (Unit 1) contains sediment transported and deposited by glacial ice. Glaciation in northwestern Greenland abraded materials beneath the ice creating the basal till including cobble-sized clasts and fine rock flour.

2. *Retreat*: Ice retreated exposing the Camp Century area to surface processes (Christ et al., 2021, 2023). The till weathered and grain coatings formed (Christ et al., 2021, 2023). Sometime after the till weathered, Unit 2 was deposited. Unit 2 may be preserved snow/firn from an interglacial or remanent basal ice from a later glaciation.

3. *Water and vegetation*: During interglacial conditions, the permafrost landscape was subject to freeze-thaw cycles as shown by the vertical lenses of clear ice in Unit 2. Till, saturated by water, flowed downslope and buried the ice forming Unit 3. Interglacial conditions supported plant growth and the development of a headwaters fluvial system that eroded the upper portion of the flow-till deposit stripping grain coatings but not changing grain shape. The fluvial system then deposited bedded sand, initially fine-grained and then coarser-grained material.

4. *Readvance*: When the climate cooled after MIS 11, ice covered the Camp Century core site (Christ et al., 2023). This ice is currently cold-based and non-erosive.

Unit 5 (MIS 11, 416 ± 38 ka)		
Scale	Diagnostic features	Interpretation
Micro	84% of grains have little to no coating, wide distribution of grain sizes, 39% fine grained particles.	The fluvial system increases in energy enough to transport larger grain size sediment.
Meso	bedded sands, increasing in grain size toward top of unit	
Macro	39% quartz, 44% potassium feldspar, 17% plagioclase, <1% amphibole (only at the top of the unit)	

Unit 4		
Scale	Diagnostic features	Interpretation
Micro	77% of grains have little to no coating, 59% fine grained fraction, very well sorted	Low energy fluvial system deposits well-sorted fine sand over slumped till (unit 3)
Meso	fine sand with well-defined parallel sub-horizontal bedding	
Macro	74% quartz, 21% plagioclase, 5% feldspar	

Unit 3		
Scale	Diagnostic features	Interpretation
Micro	14% of grains have substantial coatings, samples lower in unit have more coatings, 40% fine grained particles	Interglacial conditions. The presence of liquid causes the upper portion of the subglacial till to slump over the remaining ice (unit 2), creating a flow till deposit with normal grading.
Meso	upper samples have high ice content with near vertical bedding, larger grains in the lower portion where bedforms are not visible	
Macro	66% quartz, 18% plagioclase, 10% feldspar, 6% pyroxene	

Unit 2		
Scale	Diagnostic features	Interpretation
Micro	56% of grains have substantial coating, 78% fine-grained particles	Sediment laden ice (basal ice or firn) that survived interglacial conditions. Freeze-thaw cycles caused vertical fractures that filled with water that refroze.
Meso	>80% ice content with disseminated particles arranged in sub-horizontal bands, vertical fractures of clear ice	
Macro	75% quartz, 18% plagioclase, 7% potassium feldspar	

Unit 1 (>1.4 to <3.2 ± 0.4 Ma)		
Scale	Diagnostic features	Interpretation
Micro	63% of grains have substantial coating, 46% fine-grained particles	Subglacial till weathered in place and resulting from prior glaciation that eroded the landscape
Meso	poor sorting, sub-horizontal ice lenses, matrix supported, no clear bedding	
Macro	57% quartz, 22% plagioclase, 12% potassium feldspar, 6% pyroxene, <2% Clay	

Figure 8. Proposed sequence of events that led to the accumulation of the 5 units. Diagnostic features summarized by scale of observation. Time constraints based on past work (Christ et al., 2021, 2023).

5.3 Implications

625 Multiscale investigation of the Camp Century sub-glacial materials documents glacial and deglacial processes on Greenland's surface over time. Systematic use of CT scanning enhanced our ability to describe the sequence of environmental change archived in the sub-glacial material. Such meso-scale observations have led to the identification of transitions in environmental conditions, allowed us to observe internal sedimentary and cryogenic structures, and provide an archive of 3D models of the samples that no longer exist in their original state. Macro-scale XRD mineralogic observations imply consistent sourcing of

630 sedimentary material. Micro-scale data allow linkages of process-specific attributes to the meso-scale observations. Uncertainties remain regarding the explanation for intra-unit variability, the extent and duration of ice-free conditions, and the history of formation for Unit 2. Further investigation into the Camp Century archive and future collections of sub-glacial materials will refine the understanding of Greenland's paleoclimate and glaciologic history.

Data Availability

635 Raw data from this project is archived in the Arctic Database and can be cited as: *Nicolas Perdrial, Paul Bierman, & Catherine Collins. (2024). 2019 - 2025 New Analyzes of the Camp Century Basal Sediment (Greenland): Mineralogy, Microscopy, Computer Tomography of the bottom 340cm of the core divided in 26 subsamples. Arctic Data Center. urn:uuid:2f6ee0ff-7444-4a76-85c4-909daac4312a.* (note that this is a preliminary citation.)

640 3D visualizations of the μCT scans are available for viewing and download in an online public repository:
https://www.morphosource.org/concern/cultural_heritage_objects/000583438

645 **Author Contributions**

C. C., N. P., P. R. B., P-H., B., N.K.: Study design, data production, analysis, data interpretation, writing. C. C., N. P., P-H. B., N. K., P.C.K., Grain analysis, scanning electron microscopy data acquisition. P-H. B, W. C. M., Y. M., unpolished micro-

scale SEM data acquisition and interpretation. C. C., H. M., J. S., Sample handling. C. C.: Computed tomography scan acquisition. P.R.B, P.C.B, N.P., Funding acquisition.

650 **Competing Interests**

Paul R. Bierman is an editor on the special issue: Camp Century ice and sediment core: new science from a 1966 core that touched the base of the Greenland ice sheet (CP/TC inter-journal SI)

References

660   Anderberg, M. R. (1973). *Cluster Analysis for Applications*. Elsevier. https://doi.org/10.1016/C2013-0-06161-0

Bader, H. (1962). Scope, Problems, and Potential Value of Deep Core Drilling in Ice Sheets. *CRREL Special Report 58*, 1–17.

Balter-Kennedy, A., Schaefer, J. M., Briner, J. P., Young, N. E., Walcott, C., Kuhl, T., Moravec, E., Keisling, B. A., Anandakrishnan, S., Stevens, N., & Brown, N. (2023). First Results from GreenDrill: Exposure dating in sub-ice material from Prudhoe Dome, northwestern Greenland. *(C14A-07) Presented at AGU23.*

665   Bender, M. L., Burgess, E., Alley, R. B., Barnett, B., & Clow, G. D. (2010). On the nature of the dirty ice at the bottom of the GISP2 ice core. *Earth and Planetary Science Letters*, *299*(3–4), 466–473. https://doi.org/10.1016/J.EPSL.2010.09.033

Bierman, P. R., Christ, A. J., Collins, C. M., Mastro, H. M., Souza, J., Blard, P.-H., Brachfeld, S., Courville, Z. R., Rittenour, T. M., Thomas, E. K., Tison, J.-L., & Fripiat, F. (2024). Scientific history, sampling approach, and physical characterization of the Camp Century sub-glacial sediment core, a rare archive from beneath the Greenland Ice Sheet

670   [Manuscript under review]. *The Cryosphere*.

Bierman, P. R., Corbett, L. B., Graly, J. A., Neumann, T. A., Lini, A., Crosby, B. T., & Rood, D. H. (2014). Preservation of a Preglacial Landscape Under the Center of the Greenland Ice Sheet. *Science*, *344*(6182), 402–405. https://doi.org/10.1126/science.1249047

Bierman, P. R., Steig, E. J., Mastro, H. M., Corbett, L., Caffee, M., Hidy, Alan., & Halsted, C. (2023). Fossil vegetation and

675   26Al/10Be in basal till from GISP2 core further constrain existing interpretations of ice sheet history in central Greenland. *American Geophysical Union Fall Meeting.*, *C11D-1068.*

Blard, P. H., Protin, M., Tison, J. L., Fripiat, F., Dahl-Jensen, D., Steffensen, J. P., Mahaney, W. C., Bierman, P. R., Christ, A. J., Corbett, L. B., Debaille, V., Rigaudier, T., & Claeys, P. (2023). Basal debris of the NEEM ice core, Greenland: a window into sub-ice-sheet geology, basal ice processes and ice-sheet oscillations. *Journal of Glaciology*, *268*(11).

680   https://doi.org/10.1017/jog.2022.122

Brevik, E. C., & Reid, J. R. (2000). Differentiating Till and Debris Flow Deposits in Glacial Landscapes. *Soil Horizons*, *41*(3), 83. https://doi.org/10.2136/sh2000.3.0083

Briner, J. P., Walcott, C. K., Schaefer, J. M., Young, N. E., MacGregor, J. A., Poinar, K., Keisling, B. A., Anandakrishnan, S., Albert, M. R., Kuhl, T., & Boeckmann, G. (2022). Drill-site selection for cosmogenic-nuclide exposure dating of the

685   bed of the Greenland Ice Sheet. *The Cryosphere*, *16*(10), 3933–3948. https://doi.org/10.5194/tc-16-3933-2022

Cailleux, A., & Tricart, J. (1959). *Initiation à l'étude des sables et des galets: Vol. Vol 5*. CDU.

Calmels, F., & Allard, M. (2008). Segregated Ice Structures in Various Heaved Permafrost Landforms Through CT Scan. *Earth Surf. Process. Landforms*, *33*, 209–225. https://doi.org/10.1002/esp

Christ, A. J., Bierman, P. R., Schaefer, J. M., Dahl-Jensen, D., Steffensen, J. P., Corbett, L. B., Peteet, D. M., Thomas, E. K.,

690   Steig, E. J., Rittenour, T. M., Tison, J.-L., Blard, P.-H., Perdrial, N., Dethier, D. P., Lini, A., Hidy, A. J., Caffee, M. W.,

& Southon, J. (2021). A multimillion-year-old record of Greenland vegetation and glacial history preserved in sediment beneath 1.4 km of ice at Camp Century. *PNAS*, *118*(13). https://doi.org/10.1073/pnas.2021442118/-/DCSupplemental

Christ, A. J., Rittenour, T. M., Bierman, P. R., Keisling, B. A., Knutz, P. C., Thomsen, T. B., Keulen, N., Fosdick, J. C., Hemming, S. R., Tison, J.-L., Blard, P.-H., Steffensen, J. P., Caffee, M. W., Corbett, L. B., Dahl-Jensen, D., Dethier, D.
695   P., Hidy, A. J., Perdrial, N., Peteet, D. M., … Thomas, E. K. (2023). Deglaciation of northwestern Greenland during Marine Isotope Stage 11. *Science*, *381*(6655), 330–335. https://doi.org/10.1126/science.ade4248

Clark, E. F. (1965). *Camp Century Evolution of Concept and History of Design Construction and Performance*.

Dixon, J. C., Thorn, C. E., Darmody, R. G., & Campbell, S. W. (2002). Weathering rinds and rock coatings from an Arctic alpine environment, northern Scandinavia. *Geological Society of America Bulletin*, *114*(2), 226–238.
700   https://doi.org/10.1130/0016-7606(2002)114<0226:WRARCF>2.0.CO;2

Dutton, A., Carlson, A. E., Long, A. J., Milne, G. A., Clark, P. U., DeConto, R., Horton, B. P., Rahmstorf, S., & Raymo, M. E. (2015). Sea-level rise due to polar ice-sheet mass loss during past warm periods. *Science*, *349*(6244). https://doi.org/10.1126/science.aaa4019

Emmanouilidis, A., Messaris, G., Ntzanis, E., Zampakis, P., Prevedouros, I., Bassukas, D. A., & Avramidis, P. (2020). CT
705   scanning, X-ray fluorescence: Non-destructive techniques for the identification of sedimentary facies and structures. *Revue de Micropaleontologie*, *67*. https://doi.org/10.1016/j.revmic.2020.100410

Fountain, J., Usselman, T. M., Wooden, J., & Langway, C. C. (1981). Evidence of the Bedrock Beneath the Greenland Ice Sheet Near Camp Century, Greenland. *Journal of Glaciology*, *27*(95), 193–197. https://doi.org/10.3189/S0022143000011370

710   French, H., & Shur, Y. (2010). The principles of cryostratigraphy. *Earth-Science Reviews*, *101*(3–4), 190–206. https://doi.org/10.1016/j.earscirev.2010.04.002

Garzanti, E. (2017). The Maturity Myth In Sedimentology and Provenance Analysis. *Journal of Sedimentary Research*, *87*(4), 353–365. https://doi.org/10.2110/jsr.2017.17

Gemery, L., & López-Quirós, A. (2024). Polar paleoenvironmental perspectives on modern climate change. *PLOS Climate*,
715   *3*(1), e0000333. https://doi.org/10.1371/journal.pclm.0000333

Gilbert, G. L., Kanevskiy, M., & Murton, J. B. (2016). Recent Advances (2008–2015) in the Study of Ground Ice and Cryostratigraphy. *Permafrost and Periglacial Processes*, *27*(4), 377–389. https://doi.org/10.1002/ppp.1912

Goldich, S. S. (1938). A Study in Rock-Weathering. *The Journal of Geology*, *46*(1), 17–58. https://doi.org/10.1086/624619

Gow, A. J., & Meese, D. A. (1996). Nature of basal debris in the GISP2 and Byrd ice cores and its relevance to bed processes.
720   *Annals of Glaciology*, *22*, 134–140. https://doi.org/10.3189/1996AoG22-1-134-140

Gow, A. J., Meese, D. A., Alley, R. B., Fitzpatrick, J. J., Anandakrishnan, S., Woods, G. A., & Elder, B. C. (1997). Physical and structural properties of the Greenland Ice Sheet Project 2 ice core: A review. *Journal of Geophysical Research: Oceans*, *102*(C12), 26559–26575. https://doi.org/10.1029/97JC00165

Gregersen, U., Knutz, P. C., Pedersen, G. K., Nøhr-Hansen, H., Ineson, J. R., Larsen, L. M., Hopper, J. R., Bojesen-Koefoed, J. A., Dam, G., Funck, T., & Hovikoski, J. (2022). *Stratigraphy of the West Greenland Margin*. https://doi.org/10.4095/321849

Gresina, F., Farkas, B., Fábián, S. Á., Szalai, Z., & Varga, G. (2023). Morphological analysis of mineral grains from different sedimentary environments using automated static image analysis. *Sedimentary Geology*, *455*, 106479. https://doi.org/10.1016/j.sedgeo.2023.106479

Hambreky, M. J., Bennett, M. R., Dowdeswell, J. A., Glasser, N. F., & Huddart, D. (1999). Debris entrainment and transfer in polythermal valley glaciers. *Journal of Glaciology*, *45*(149), 69–86. https://doi.org/10.3189/S0022143000003051

Hansen, B. L., & Langway, C. C. (1966a). Deep Core Drilling in Ice and Core Analysis at Camp Century, Greenland, 1961-1966. *Antarctic Journal of the United States* , *1*(5), 207–208.

Hansen, B. L., & Langway, C. C. (1966b). *Glaciology Deep Core Drilling in Ice and Core Analysis at Camp Century, Greenland, 1961-1966*.

Harrison, J. C., St-Onge, M. R., Petrov, O. V, Strelnikov, S. I., Lopatin, B. G., Wilson, F. H., Tella, S., Paul, D., Lynds, T., Shokalsky, S. P., Hults, C. K., Bergman, S., Jepsen, H. F., & Solli, A. (2011). Geological map of the Arctic. *Geological Survey of Canada*, *"A" Series Map*(2159A). https://doi.org/10.4095/287868

Harwood, D. M. (1986). Do Diatoms beneath the Greenland Ice Sheet Indicate Interglacials Warmer than Present? *Arctic*, *39*(4), 304–308.

Herron, S., Hoar, & Langway, C. C. (1979). The Debris-Laden Ice at the Bottom of the Greenland Ice Sheet. *Journal of Glaciology*, *23*(89), 193–207. https://doi.org/10.3189/s002214300002983x

Hjulström, F. (1935). *Studies of the morphological activity of rivers as illustrated by the River Fyris*. Uppsala University.

Janoo, V. C. (1998). Quantification of Shape, Angularity, and Surface texture of Base Course Materials. *US Transportation Collection*.

Jansson, N. F., Allen, R. L., Skogsmo, G., & Tavakoli, S. (2022). Principal component analysis and K-means clustering as tools during exploration for Zn skarn deposits and industrial carbonates, Sala area, Sweden. *Journal of Geochemical Exploration*, *233*, 106909. https://doi.org/10.1016/j.gexplo.2021.106909

JMP (Version 18.0). (2024). SAS Institute Inc.

Johnsen, S. J., Dansgaard, W., Clausen, H. B., & Lang Way, C. C. (1972). Oxygen Isotope Profiles through the Antarctic and Greenland Ice Sheets. In *Biochem. Biophys. Res. Commun* (Vol. 235).

Jouzel, J., Masson-Delmotte, V., Cattani, O., Dreyfus, G., Falourd, S., Hoffmann, G., Minster, B., Nouet, J., Barnola, J. M., Chappellaz, J., Fischer, H., Gallet, J. C., Johnsen, S., Leuenberger, M., Loulergue, L., Luethi, D., Oerter, H., Parrenin, F., Raisbeck, G., … Wolff, E. W. (2007). Orbital and Millennial Antarctic Climate Variability over the Past 800,000 Years. *Science*, *317*(5839), 793–796. https://doi.org/10.1126/science.1141038

Kalińska-Nartiša, E., Stivrins, N., & Grudzinska, I. (2018). Quartz grains reveal sedimentary palaeoenvironment and past storm events: A case study from eastern Baltic. *Estuarine, Coastal and Shelf Science*, *200*, 359–370. https://doi.org/10.1016/j.ecss.2017.11.027

Keulen, N., Malkki, S. N., & Graham, S. (2020). Automated Quantitative Mineralogy Applied to Metamorphic Rocks. *Minerals*, *10*(1), 47. https://doi.org/10.3390/min10010047

Knight, P. G. (1997). The basal ice layer of glaciers and ice sheets. *Quaternary Science Reviews*, *16*(9), 975–993. https://doi.org/10.1016/S0277-3791(97)00033-4

Krumbein, W. C. (1941). The Effects of Abrasion on the Size, Shape and Roundness of Rock Fragments. *The Journal of Geology*, *49*(5), 482–520. https://doi.org/10.1086/624985

Kuenen, P. H. (1959). Experimental abrasion; 3, Fluviatile action on sand. *American Journal of Science*, *257*(3), 172–190. https://doi.org/10.2475/ajs.257.3.172

Langway, C. C. (2008). The History of Early Polar Ice Cores. *Cold Regions Science and Technology*, *52*(2), 101–117. https://doi.org/10.1016/j.coldregions.2008.01.001.

Langway, C. C., & Hansen, B. L. (1970). Drilling Through the Ice Cap: Probing Climate for a Thousand Centuries. *Bulletin of the Atomic Scientists*, *26*(10), 62–66.

Lapalme, C. M., Lacelle, D., Pollard, W., Fortier, D., Davila, A., & McKay, C. P. (2017). Cryostratigraphy and the Sublimation Unconformity in Permafrost from an Ultraxerous Environment, University Valley, McMurdo Dry Valleys of Antarctica. *Permafrost and Periglacial Processes*, *28*(4), 649–662. https://doi.org/10.1002/ppp.1948

Lee, A. S., Enters, D., Titschack, J., & Zolitschka, B. (2021). Facies characterisation of sediments from the East Frisian Wadden Sea (Germany): New insights from down-core scanning techniques. *Geologie En Mijnbouw/Netherlands Journal of Geosciences*. https://doi.org/10.1017/njg.2021.6

Lei, L., Park, T., Jarvis, K., Pan, L., Tepecik, I., Zhao, Y., Ge, Z., Choi, J.-H., Gai, X., Galindo-Torres, S. A., Boswell, R., Dai, S., & Seol, Y. (2022). Pore-scale observations of natural hydrate-bearing sediments via pressure core sub-coring and micro-CT scanning. *Scientific Reports*, *12*(1), 3471. https://doi.org/10.1038/s41598-022-07184-6

Lei, L., Seol, Y., & Jarvis, K. (2018). Pore-Scale Visualization of Methane Hydrate-Bearing Sediments With Micro-CT. *Geophysical Research Letters*, *45*(11), 5417–5426. https://doi.org/10.1029/2018GL078507

Lepp, A. P., Miller, L. E., Anderson, J. B., O'Regan, M., Winsborrow, M. C. M., Smith, J. A., Hillenbrand, C.-D., Wellner, J. S., Prothro, L. O., & Podolskiy, E. A. (2024). Insights into glacial processes from micromorphology of silt-sized sediment. *The Cryosphere*, *18*(5), 2297–2319. https://doi.org/10.5194/tc-18-2297-2024

Lisiecki, L. E., & Raymo, M. E. (2005). A Pliocene-Pleistocene stack of 57 globally distributed benthic δ18O records. *Paleoceanography*, *20*(1), 1–17. https://doi.org/10.1029/2004PA001071

Lüthi, D., Le Floch, M., Bereiter, B., Blunier, T., Barnola, J.-M., Siegenthaler, U., Raynaud, D., Jouzel, J., Fischer, H., Kawamura, K., & Stocker, T. F. (2008). High-resolution carbon dioxide concentration record 650,000–800,000 years before present. *Nature*, *453*(7193), 379–382. https://doi.org/10.1038/nature06949

790   Mackowiak, T. J., & Perdrial, N. (2023). Monitoring of Suspended Sediment Mineralogy in Puerto-Rican Rivers: Effects of Flowrate and Lithology. *Minerals*, *13*(2), 208. https://doi.org/10.3390/min13020208

Mahaney, W. C. (2002). *Atlas of Sand Grain Surface Textures and Applications*. Oxford University Press.

Malusà, M. G., Resentini, A., & Garzanti, E. (2016). Hydraulic sorting and mineral fertility bias in detrital geochronology. *Gondwana Research*, *31*, 1–19. https://doi.org/10.1016/j.gr.2015.09.002

795   Marschalek, J. W., Blard, P. -H., Sarigulyan, E., Ehrmann, W., Hemming, S. R., Thomson, S. N., Hillenbrand, C. -D., Licht, K., Tison, J. -L., Ardoin, L., Fripiat, F., Allen, C. S., Marrocchi, Y., Siegert, M. J., & van de Flierdt, T. (2024). Byrd Ice Core Debris Constrains the Sediment Provenance Signature of Central West Antarctica. *Geophysical Research Letters*, *51*(5). https://doi.org/10.1029/2023GL106958

Mena, A., Francés, G., Pérez-Arlucea, M., Aguiar, P., Barreiro-Vázquez, J. D., Iglesias, A., & Barreiro-Lois, A. (2015). A
800   novel sedimentological method based on CT-scanning: Use for tomographic characterization of the Galicia Interior Basin. *Sedimentary Geology*, *321*, 123–138. https://doi.org/10.1016/j.sedgeo.2015.03.007

Moon, T. A., Fisher, M., Stafford, T., & Thurber, A. (2023). QGreeland (v3.0.0) [dataset]. In *National Snow and Ice Data Center*.

Murton, J. B., & French, H. M. (1994). Cryostructures in permafrost, Tuktoyaktuk coastlands, western arctic Canada.
805   *Canadian Journal of Earth Sciences*, *31*(4), 737–747. https://doi.org/10.1139/e94-067

Musselman, Z. A., & Tarbox, A. M. (2013). Downstream Trends in Grain Size, Angularity, and Sorting of Channel-Bed and Bank Deposits in a Coastal Plain Sand-Bed River: the Pascagoula River System, Mississippi, USA. *Southeastern Geographer*, *53*(2), 177–197. https://doi.org/10.1353/sgo.2013.0017

Naqshband, S., & McElroy, B. (2016). Sediment transport at grain scale: A review, future research and morphological
810   implications. *River Flow 2016*, 914–918. https://doi.org/10.1201/9781315644479-145

Nitzbon, J., Gadylyaev, D., Schlüter, S., Köhne, J. M., Grosse, G., & Boike, J. (2022). Brief communication: Unravelling the composition and microstructure of a permafrost core using X-ray computed tomography. *The Cryosphere*, *16*(9), 3507–3515. https://doi.org/10.5194/tc-16-3507-2022

Orsi, T. H., Edwards, C. M., & Anderson', A. L. (1994). X-Ray Computed Tomography: A Non-destructive Method for
815   Quantitative Analysis of Sediment Cores. *Journal of Sedimentary Research*, *64A*(3), 690–693. http://pubs.geoscienceworld.org/sepm/jsedres/article-pdf/64/3a/690/2812031/690.pdf

Perdrial, N., Collins, C. M., & Bierman, P. R. (2024). 2019 - 2025 New Analyzes of the Camp Century Basal Sediment (Greenland): Mineralogy, Microscopy, Computer Tomography of the bottom 340cm of the core divided in 26 subsamples. In *Arctic Data Center*.

820   Pesch, C., Weber, P. L., Moldrup, P., de Jonge, L. W., Arthur, E., & Greve, M. H. (2022). Physical characterization of glacial rock flours from fjord deposits in South Greenland–Toward soil amendment. *Soil Science Society of America Journal*, *86*(2), 407–422. https://doi.org/10.1002/saj2.20352

R Core Team. (2022). *R: A Language and Environment for Statistical Computing* (4.2.2). R Foundation for Statistical Computing.

825 Razi, T., Niknami, M., & Alavi Ghazani, F. (2014). Relationship between Hounsfield Unit in CT Scan and Gray Scale in CBCT. *Journal of Dental Research, Dental Clinics, Dental Prospects*, *8*(2), 107–110. https://doi.org/10.5681/joddd.2014.019

Renter, J. A. M. (1989). Applications of computerized tomography in sedimentology. *Marine Geotechnology*, *8*(3), 201–211. https://doi.org/10.1080/10641198909379868

830 Rietveld, H. M. (1969). A profile refinement method for nuclear and magnetic structures. *Journal of Applied Crystallography*, *2*(2), 65–71. https://doi.org/10.1107/S0021889869006558

Robinson, A., Alvarez-Solas, J., Calov, R., Ganopolski, A., & Montoya, M. (2017). MIS-11 duration key to disappearance of the Greenland ice sheet. *Nature Communications*, *8*(1), 16008. https://doi.org/10.1038/ncomms16008

Schaefer, J. M., Finkel, R. C., Balco, G., Alley, R. B., Caffee, M. W., Briner, J. P., Young, N. E., Gow, A. J., & Schwartz, R.
835 (2016). Greenland was nearly ice-free for extended periods during the Pleistocene. *Nature*, *540*(7632), 252–255. https://doi.org/10.1038/nature20146

Schindelin, J., Arganda-Carreras, I., Frise, E., Kaynig, V., Longair, M., Pietzsch, T., Preibisch, S., Rueden, C., Saalfeld, S., Schmid, B., Tinevez, J.-Y., White, D. J., Hartenstein, V., Eliceiri, K., Tomancak, P., & Cardona, A. (2012). Fiji: an open-source platform for biological-image analysis. *Nature Methods*, *9*(7), 676–682. https://doi.org/10.1038/nmeth.2019

840 Souchez, R., Bouzette, A., Clausen, H. B., Johnsen, S. J., & Jouzel, J. (1998). A stacked mixing sequence at the base of the Dye 3 core, Greenland. *Geophysical Research Letters*, *25*(10), 1943–1946. https://doi.org/10.1029/98gl01411

Souchez, R., Janssens, L., Lemmens, M., & Stauffer, B. (1995). Very low oxygen concentration in basal ice from Summit, central Greenland. *Geophysical Research Letters*, *22*(15), 2001–2004. https://doi.org/10.1029/95GL01995

Souchez, R., Tison, J. -L, Lorrain, R., Lemmens, M., Janssens, L., Stievenard, M., Jouzel, J., Sveinbjörnsdottir, A., & Johnsen,
845 S. J. (1994). Stable isotopes in the basal silty ice preserved in the Greenland Ice Sheet at summit; environmental implications. *Geophysical Research Letters*, *21*(8), 693–696. https://doi.org/10.1029/94GL00641

Stephani, E., Fortier, D., Shur, Y., Fortier, R., & Doré, G. (2014). A geosystems approach to permafrost investigations for engineering applications, an example from a road stabilization experiment, Beaver Creek, Yukon, Canada. *Cold Regions Science and Technology*, *100*, 20–35. https://doi.org/10.1016/j.coldregions.2013.12.006

850 Suwa, M., von Fischer, J. C., Bender, M. L., Landais, A., & Brook, E. J. (2006). Chronology reconstruction for the disturbed bottom section of the GISP2 and the GRIP ice cores: Implications for Termination II in Greenland. *Journal of Geophysical Research Atmospheres*, *111*(2). https://doi.org/10.1029/2005JD006032

Szmańda, J. B., & Witkowski, K. (2021). Morphometric Parameters of Krumbein Grain Shape Charts—A Critical Approach in Light of the Automatic Grain Shape Image Analysis. *Minerals*, *11*(9), 937. https://doi.org/10.3390/min11090937

855   Tafesse, S., Robison Fernlund, J. M., Sun, W., & Bergholm, F. (2013). Evaluation of image analysis methods used for quantification of particle angularity. *Sedimentology*, *60*(4), 1100–1110. https://doi.org/10.1111/j.1365-3091.2012.01367.x

Tison, J., Thorsteinsson, T., & Lorrain, R. (1994). EPSL Origin and development of textures and fabrics in basal ice at Summit, Central Greenland. *Earth and Planetary Science Letters*, *125*, 421–437.

860   van Hateren, J. A., van Buuren, U., Arens, S. M., van Balen, R. T., & Prins, M. A. (2020). Identifying sediment transport mechanisms from grain size–shape distributions, applied to aeolian sediments. *Earth Surface Dynamics*, *8*(2), 527–553. https://doi.org/10.5194/esurf-8-527-2020

Vandel, E., Vaasma, T., & Sugita, S. (2020). Application of image analysis technique for measurement of sand grains in sediments. *MethodsX*, *7*, 100981. https://doi.org/10.1016/j.mex.2020.100981

865   Vandenberghe, J., & Nugteren, G. (2001). Rapid climatic changes recorded in loess successions. *Global and Planetary Change*, *28*(1–4), 1–9. https://doi.org/10.1016/S0921-8181(00)00060-6

Voosen, P. (2019). Mud in storied ice core hints at a thawed Greenland. *Science*, *366*(6465), 556–557. https://doi.org/10.1126/science.366.6465.556

W. Dansgaard, S. J. Johnsen, J. Moller, & C. C. Langway Jr. (1969). One Thousand Centuries of Climatic Record from Camp
870   Century on the Greenland Ice Sheet. *Science*.

Whalley, W. B., & Langway, C. C. (1980). A Scanning Electron Microscope Examination of Subglacial Quartz Grains from Camp Century Core, Greenland–A Preliminary Study. *Journal of Glaciology*, *25*(91), 125–132. https://doi.org/10.3189/s0022143000010340

Willerslev, E., Cappellini, E., Boomsma, W., Nielsen, R., Hebsgaard, M. B., Brand, T. B., Hofreiter, M., Bunce, M., Poinar,
875   H. N., Dahl-Jensen, D., Johnsen, S., Steffensen, J. P., Bennike, O., Schwenninger, J.-L., Nathan, R., Armitage, S., de Hoog, C.-J., Alfimov, V., Christl, M., … Collins, M. J. (2007). Ancient Biomolecules from Deep Ice Cores Reveal a Forested Southern Greenland. *Science*, *317*(5834), 111–114. https://doi.org/10.1126/science.1141758

Woronko, B., Pisarska-Jamroży, M., & Loon, A. J. (Tom) van. (2015). Reconstruction of sediment provenance and transport processes from the surface textures of quartz grains from Late Pleistocene sandurs and an ice-marginal valley in NW
880   Poland. *Geologos*, *21*(2), 105–115. https://doi.org/10.1515/logos-2015-0007

Yau, A. M., Bender, M. L., Blunier, T., & Jouzel, J. (2016). Setting a chronology for the basal ice at Dye-3 and GRIP: Implications for the long-term stability of the Greenland Ice Sheet. *Earth and Planetary Science Letters*, *451*, 1–9. https://doi.org/10.1016/J.EPSL.2016.06.053